Volumetric velocimetry for fluid flows

Stefano Discetti[1*], Filippo Coletti[2]

* Corresponding author: sdiscett@ing.uc3m.es

1 Aerospace Engineering Group, Universidad Carlos III de Madrid, Leganés, Spain
2 Aerospace Engineering and Mechanics, University of Minnesota, Minneapolis, USA

Abstract

In the last two decades, several techniques have been introduced that are capable to extract three-dimensional three-components velocity fields in fluid flows. Fast-paced developments in both hardware and processing algorithms have generated a diverse collection of methods, with a growing range of application in flow diagnostics. The context has been further enriched by an increasingly marked trend of hybridization, in which the boundaries between different techniques are fading. In this review, we carry out a survey of the prominent methods, including optical techniques and approaches based on medical imaging. Each one is outlined through a sample application from the recent literature, focusing on respective strengths and challenges. A framework for the evaluation of the velocimetry performance in terms of dynamic spatial range is discussed, along with technological trends and emerging strategies to exploit 3D data. While critical challenges still exist, these observations highlight how volumetric techniques are transforming experimental fluid mechanics, and that the possibilities they offer have just begun to be explored.

1. Introduction

The inherent three-dimensional (3D) nature of most fluid flows requires suitable tools for their detailed measurement. Yet, until relatively recently only single-point or at best planar techniques for velocity measurements have been available to the experimentalist. Most often researchers have had to live with somewhat questionable assumptions of flow homogeneity in one or more spatial directions. The benefits include simpler experimental setups, and more straightforward data analysis and processing. Sometimes, this approach yields rewarding results. It has long been clear, however, that to gain in-depth understanding of complex flows in both natural and man-made settings, the reconstruction of the full volumetric (3D-3C, i.e. three-dimensional and three-component) velocity field is essential. A classic example is the vortex stretching

1

mechanism in turbulent flows, which plays a key role in the transport of vorticity along the spectral pipeline of the turbulent scales. This process is essentially three-dimensional, thus one- or two-dimensional techniques such as hot-wire anemometry and planar Particle Image Velocimetry (PIV) cannot capture it in full. This fundamental difficulty extends, albeit in different forms, to countless industrial, biological, and environmental flows.

Following the strong desire for 3D measurements, a number of volumetric velocimetry methods have flourished over the last decades. In part, this has followed the evolution of techniques already used in experimental fluid mechanics, especially particle-based velocimetry. In part, however, the progress has been accelerated by concepts and technologies borrowed from adjacent fields, including computer vision and medical imaging. It is now evident that the advent of tomographic particle image velocimetry (Tomographic PIV, Elsinga et al. 2006) has represented a turning point in experimental fluid mechanics, with an explosion of applications especially in turbulent flows, and it has fueled advancements even in established volumetric techniques such as 3D Particle Tracking Velocimetry (3D PTV, Maas et al. 1993) and Holographic PIV (Hinsch 2002). Additionally, the availability of more powerful and affordable computers allowed acquiring and handling larger amounts of data, which was necessary for the extension to 3D (see the discussion on the technological drivers in Sec. 3.3). In parallel, the continuous progress in medical imaging technology has led to the refinement of 3D flow measurements by non-optical methods, in particular based on Magnetic Resonance Imaging (MRI, Elkins & Alley 2007, Markl et al. 2012).

These advances have paved the way towards novel research trajectories whose merits have immediately become apparent, and which are likely to remain productive for a long time. The 3D information extraction, however, requires the introduction of novel measurement paradigms, concerning both the design and execution of experiments. It also comes at the cost of significant technical challenges, which have only partially been addressed. Indeed, the strive towards accurate flow diagnostics capable to provide full volumetric (and ideally time-resolved) information, while attaining sufficient dynamic and spatial range, represents an extremely active area of research.

The potential reward is enormous. The benefit of high-quality 3D velocity measurements is not only limited to the description of turbulent flows. Volumetric velocimetry is also essential to characterize the flow around and inside complex objects, and to validate numerical simulations thereof, while providing new opportunities to evaluate quantities which have so far eluded the experimentalist. For example, in the last years several strategies have been proposed to extract 3D pressure fields from volumetric velocity measurements, e.g. to identify aeroacoustic noise sources (van Oudheusden 2013).

Considering the above, the aim of the proposed review is twofold. On the one hand, for the same general goal of measuring 3D velocity fields, several approaches are available today and it is not trivial to identify the most suitable

one for a specific application. Our first objective is thus to provide a critical assessment of the existing volumetric velocimetry techniques. The description will be limited to the fundamentals, with the reader being referred to dedicated reviews for further details. The techniques will be illustrated through sample applications from the recent literature, to highlight respective strengths and challenges. On the other hand, the portfolio of methods has evolved rapidly in the last decade, with the introduction of new techniques and the fast improvement of others, as testified by the intense scientific production in recent years. The second objective is then to discuss the existing approaches in terms of their potential growth and application in the near future, and to identify new perspectives that emerge from the most recent implementations.

Without claiming to be exhaustive, we will focus on techniques that are now established as valuable tools for the scientific community, and at the same time show potential for further developments. In the absence of accepted classification criteria, establishing an appropriate order of presentation is not trivial. Even a chronological order is not easy to determine, because some methods do not have a precise date of birth, and have evolved over relatively long times. Therefore, we follow a (somewhat arbitrary) logical order that facilitates the exposition. We begin with 3D PTV, which has evolved into Lagrangian Particle Tracking using high-speed imaging and whose spatial resolution has recently been pushed to new heights. We then address Tomographic PIV, which since its introduction has generated an interest in the fluid mechanics community only comparable to its planar counterpart, quickly progressing through many contributions from research groups around the world. We discuss Scanning PIV, originally conceived as a planar method made volumetric by assuming a "frozen" flow, but which is increasingly used in a hybrid scanning-tomography mode. 3D Holographic velocimetry is discussed in the context of its digital in-line version, especially in light of recent efforts to overcome longstanding limitations while maintaining signature features that have determined its success. Defocusing PIV is presented in its modern form, which has moved away from the original multiple-aperture implementation and towards a multiple-camera setup, while conserving its benefits in dealing with relatively large and deep volumes. Light-field imaging is the most recent addition to 3D velocimetry of fluid flows; we review some aspects that underscore its potential, as novel dedicated hardware becomes available. We conclude the showcase with Magnetic Resonance Velocimetry, a prime example of how non-optical imaging technology developed in medical physics can be applied to both biomedical and engineering fluid mechanics, offering complementary advantages with respect to laser diagnostics. The Discussion section will elaborate on criteria for classifications, but also highlight hybridization between various methods. We will expand on metrics for performance specifically applicable to volumetric measurements, and discuss technological trends and emerging approaches that exploit the latest improvements.

2. Volumetric velocimetry techniques

2.1 Lagrangian Particle Tracking

The advancements in recording hardware and the application of photogrammetry to full-volume imaging in the 90's paved the way towards the extensive application of PTV for the analysis of tracer particle trajectories (along with the velocity and acceleration along them), referred to as Lagrangian Particle Tracking (LPT). In this section, we focus on techniques exploiting only particle image positions and intensity; methods based on defocusing/aberration imaging will be treated in a dedicated section.

The earliest examples of LPT (Nishino et al. 1989, Maas et al. 1993) were based on individual particle triangulation using a set of multiple views. In these and later applications a major limit on the seeding concentration (and, consequently, on the achievable spatial resolution) arises from the ambiguity of the reconstruction process using a limited set of views, generating the so-called ghost particles. The number of ghost particles depends on the particle image density, the particle image diameter, the depth of the illuminated volume and the number of cameras. For relatively low image density (lower than N_{ppp} =0.05 particles per pixel, ppp) Discetti & Astarita (2014) proposed the relations:

$$\frac{(N_g)_{2cam}}{N_p} = N_{ppp} d_\tau^* L_z \tag{1}$$

$$\frac{(N_g)_{N_{cam}}}{N_p} = \frac{(N_g)_{2cam}}{N_p} (1 - e^{-N_s})^{N_{cam}-2} \tag{2}$$

where N_{cam} is the number of cameras, N_g and N_p are respectively the number of ghost and true particles, d_τ^* is the particle image diameter in pixels, L_z is the depth of the volume expressed in pixels, and $N_s = N_{ppp} \frac{\pi d_\tau^{*2}}{4}$ is the source density. N_{cam} indicates the number of cameras used for the reconstruction. Considering typical values (resolution of 20 pixel/mm, $L_z = 10$ mm· 20 pixel/mm= 200 pixels, $d_\tau^* = 3$ pixels), for a 3 camera system an image density of 0.005 ppp ($N_s = 0.035$) would correspond to 10% of ghost particles, while raising the image density to 0.01 ppp ($N_s = 0.07$) rises the estimate to 40%. The limitation on seeding concentration (and consequently on instantaneous spatial resolution) bounded the development of 3D LPT for long time. Nonetheless the technique has been widely used to extract Lagrangian statistics, enabling fundamental advances in turbulence research (see for instance Voth et al. 2002, Lüthi et al. 2005, Xu et al. 2014). The accuracy needed to investigate high-order statistics is achieved by exploiting the temporal information, both to determine future particle positions from previous steps (Ouellette et al. 2006) and to obtain physically smooth trajectories (Mordant et al. 2004).

In recent years, the fast development of time-resolved Tomographic PIV had the unexpected result of starting a renaissance of LPT. A first attempt to identify particles tracks and extract Lagrangian quantities from the reconstructed volumes of Tomographic PIV was carried out by Schröder et al. (2011). Later, Wieneke (2013) developed a particle-based reconstruction approach (referred as Iterative Particle Reconstruction, IPR) exploiting image matching, i.e. adding to the traditionally used particle image positions the information on their intensity. This process optimizes the matching by "shaking" the particles around their predictor position and searching for improvements on the projection matching with the original image. The technique built upon the ongoing developments on the Optical Transfer Function calibration in the field of Tomographic PIV (Schanz et al. 2012). Pushing this approach one step further, the Shake-The-Box method (STB, Schanz et al. 2016) incorporates temporal and spatial information by combining the IPR image matching process with extrapolation of known trajectories to predict particle position at subsequent time steps. Using synthetic data, the method has been shown to handle seeding densities up to 0.125 ppp with nearly no ghost particles. The particle tracks can then be used to extract dense Lagrangian statistics or highly resolved Eulerian statistics via volume binning and ensemble averaging (Schröder et al 2015, Agüera et al 2016).

The application of LPT with the STB method is outlined here by the time-resolved measurements of a periodic hill flow by Schröder et al. (2015). The experiments are performed in the water tunnel at TU Munich. The Reynolds number range is Re=8000-33000, based on the hill height and on the bulk velocity U_b=0.171-0.698 m/s. Owing to the requirements of time-resolved data to extract trajectory, LPT is indeed typically applied to relatively low-speed flows (although Novara et al. 2016 recently demonstrated a 36 m/s application using multi-pulse illumination). A volume of 90 x 20 x 94 mm[3] is imaged by six high-speed cameras (Imager pro HS 4M/PCO Dimax). The fluid is seeded with 30 µm polyamide particles, illuminated by Nd:YLF Quantronix Darwin Duo high-repetition laser (20 mJ/pulse). Owing to the limited power of high repetition rate lasers and small aperture required for proper focusing, large particle size is desirable; additionally, the light intensity is increased by back-reflecting the laser light with a mirror placed at one extremity of the investigated domain. Multi-pass amplification with two facing mirrors (Ghaemi & Scarano 2010) has been shown to further increase the light intensity up to 7 times. The light profile is also cut by a masking window to remove weak intensity tails, limiting spurious background intensity in the reconstructed images. The illumination and imaging configuration is illustrated in Figure 1. Sequences of 3000 particle images were captured at 500 Hz and 1 kHz for the lowest and the highest Reynolds number, respectively. The captured images have an average resolution of about 21.5 pixel/mm and particle image density ranging between 0.04 and 0.06 ppp, with particle image diameters of about 3 pixels.
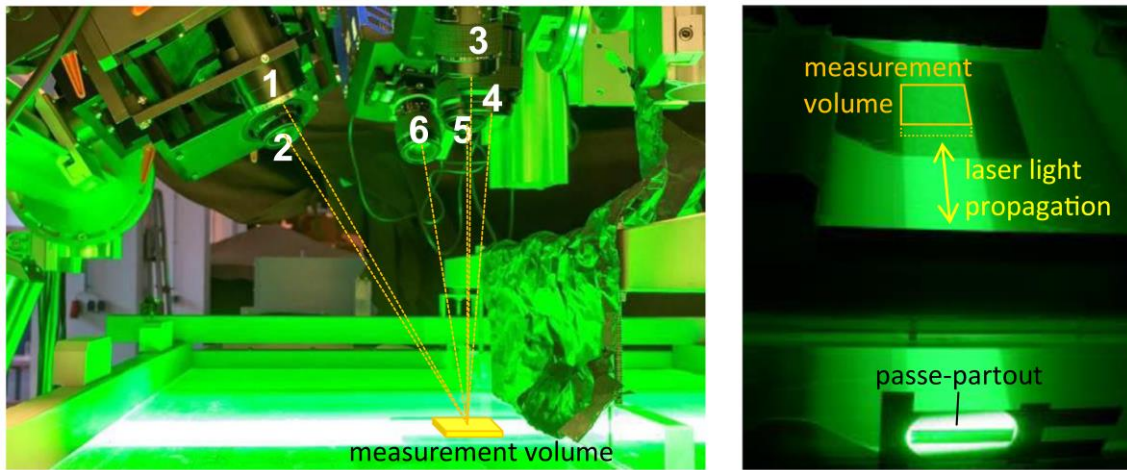
Figure 1 Imaging and illumination setup for LPT measurements of a periodic hill flow. Left: camera arrangement. Right: illumination path with black tape on the background of the imaging region. From Schröder et al. (2015). Schröder 2015 © Springer Science+Business Media Dordrecht 2015. With permission of Springer.

The optical calibration is performed with a dual-plane calibration plate, and then corrected with a volumetric self-calibration proposed by Wieneke (2008), based on the minimization of the disparity between the images of the same particle in the various camera images. The STB method is then applied; the processing steps are described in Schröder et al. (2015) and in greater detail in Schanz et al. (2016). The algorithm is divided in three phases: initialization, in which particle positions are estimated for the first few time steps, for instance via IPR, and a first set of tracks is determined; convergence, in which the trajectories are extrapolated to subsequent time steps and particle "shaking" is applied to identify new candidates; and converged phase, in which the process is iteratively repeated but the number of tracks is stable, the reconstruction changing only due to particles entering or leaving the measurement volume. Due to the extensive use of the time history information, Schröder et al. (2015) claim an uncertainty as low as 0.0033 pixels for 0.05 ppp under ideal images, and of the order of 0.1 pixels in real applications. The data are finally interpolated onto a Cartesian grid using an iterative optimization approach based on a weighted sum of 3D quadratic B-splines (Gesemann 2015). Physical constraints might also be included, for instance penalizing non-zero divergence in incompressible flows.

An example of particle tracks and vorticity isosurfaces is reported in Figure 2. Data are obtained applying the B-spline interpolation on cells 470 μm (about 10 pixels) in size. Color-coding by the streamwise component of the velocity value highlights the presence of high and low momentum regions and vortices embedded in the shear layer past the hill. Strong accelerations are detected in proximity of and inside vortex tubes.
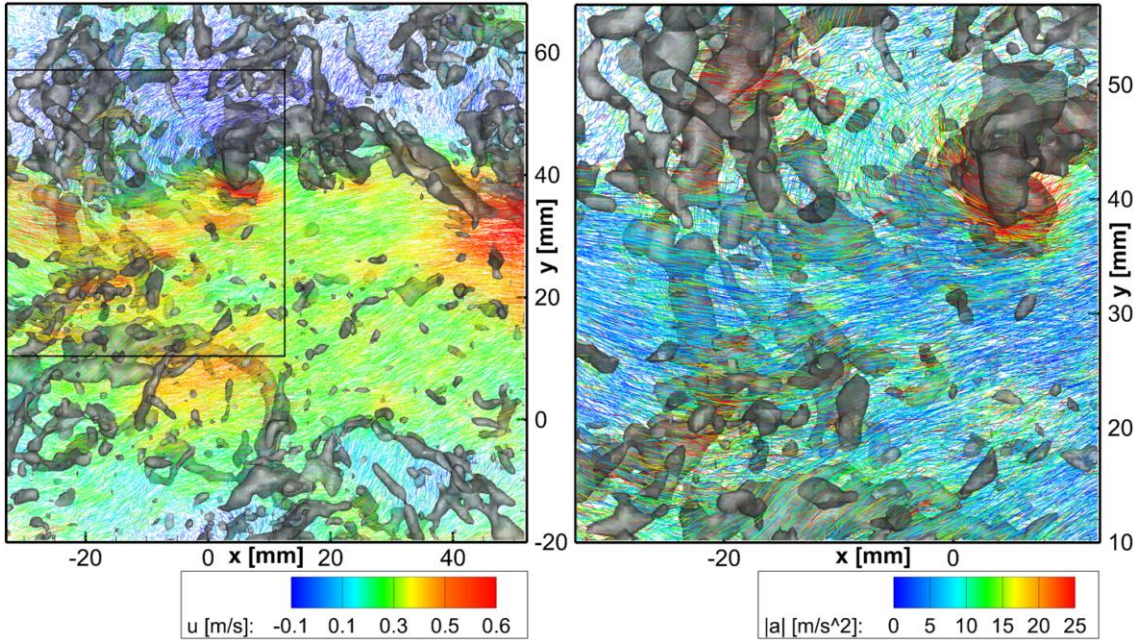
Figure 2 Lagrangian tracks over 11 time steps obtained by STB method applied to a flow past a hill. Left: color-coding with streamwise velocity and iso-contours of vorticity magnitude. Right: zoom into the box highlighted on the left panel, with track color-coded by acceleration magnitude. From Schröder et al. (2015). Schröder 2015 © Springer Science+Business Media Dordrecht 2015. With permission of Springer.

2.2   Tomographic PIV

Tomographic PIV (Elsinga et al 2006) is based on full-volume illumination and reconstruction of the light intensity field using multiple simultaneous views from different viewing directions (generally three or more cameras). The volume illumination is usually generated by expanding a laser sheet thickness along the imaging depth direction. This sets stringent requirements in terms of light intensity of the illumination, and in most cases the imaging volumes are kept to an aspect ratio between 1 : 3 and 1 : 10 (depth to in-plane size). The light intensity field is discretized into cubic compact support functions (voxels), with comparable size to that of the pixels. The imaging process is modelled as a set of linear equations, resulting from the discretization of the integral of the light intensity along the line of sight of each pixel. The unknowns to be determined are the intensity values carried by each voxel; consistency with the intensity recorded on each pixel is the condition to be enforced. Owing to the finite number of available projections (equal to the number of cameras), the reconstruction problem is ill-posed. In the early implementations, the solution of the system has been tackled using iterative algebraic methods already available in the medical imaging field (Herman & Lent 1976); however, in recent years a portfolio of features-oriented reconstruction techniques has flourished. The full three components velocity field is then computed via 3D digital cross-correlation of the reconstructed volumes (even though, owing to the larger particle spacing with respect to 2D PIV, particle tracking approaches have recently gained popularity, especially in time-resolved applications, see e.g.

7

Novara & Scarano 2013, Schneiders & Scarano 2016). The reader is referred to the review by Scarano (2013) for a detailed description of the technique.

We report an illustrative example of Tomographic PIV, highlighting several of the requirements for the successful application of the technique. The case study is the measurement by Ceglia et al. (2014) of the swirling flow issuing from a model injector for aero engine applications. The swirl injector is confined into a nine-sided methacrylate tank filled with water. The walls of the tank offer full optical access from the sides, allowing illumination by a laser slab and imaging from different directions with optical axis orthogonal to the lateral walls. A sketch of the experimental setup and injector is shown in Figure 3. The camera arrangement is selected to cover a wide angular spacing to reduce elongation of the reconstructed particles in the depth direction and to provide a set of complementary views of the particle cloud (Scarano 2013).

The flow is seeded with neutrally-buoyant polyamide particles (56 μm in diameter). The beam of a dual-cavity Gemini PIV Nd:YAG laser (200 mJ/pulse at 15 Hz) is shaped into a volume using two spherical and one cylindrical lenses. The volume thickness is shaved to 46 mm using a knife-edge mask to cut the tails of the beam profile, similar to what described in the LPT case study and common to many laser-based volumetric techniques.
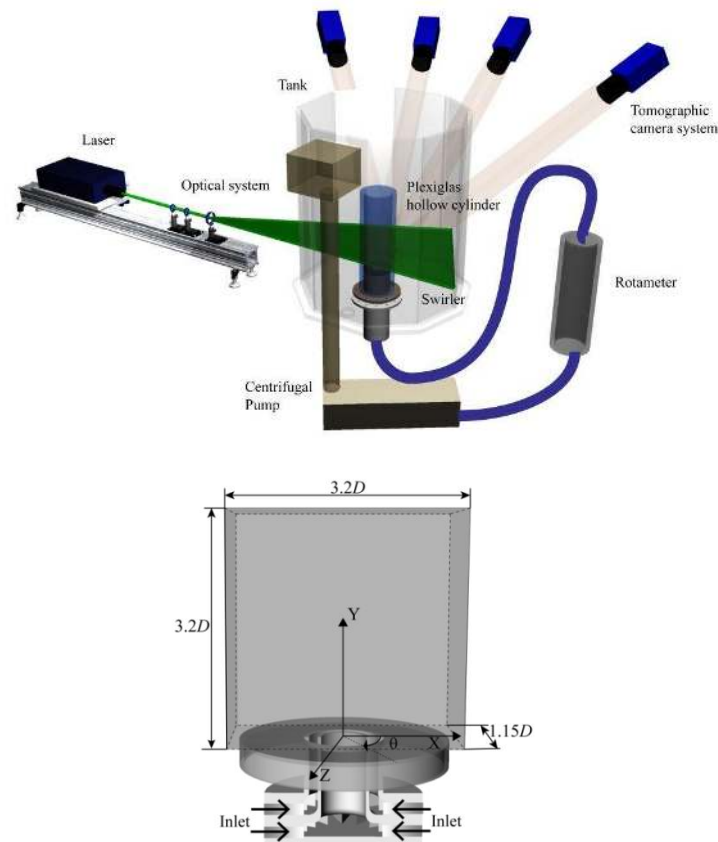

Figure 3 Top: sketch of the experimental setup to investigate a swirl flow injector with Tomographic PIV. Bottom: Schematic of the measurement domain. $D = 40mm$ is the injector exit diameter. Reprinted from Ceglia 2014, Copyright 2014, with permission from Elsevier.

The imaging system consists of a set of four LaVision Imager sCMOS 5.5 Megapixel cameras (6.5 µm pixel pitch), equipped with 100 mm EX objectives set at $f_\#$=16. A large $f_\#$ is necessary to achieve a sufficient depth of field to include the entire illuminated volume. The objectives are equipped with Scheimpflug adaptors to ensure proper focusing of the particles. Well-focused particles are indeed desirable to improve the reconstruction accuracy, even though a small blur might be acceptable (Scarano 2013). Setting similar imaging conditions for all cameras in the set (same sensor, lensing, forward/backward scattering, etc.) is not a fundamental prerequisite, but it is beneficial for consistent processing and is common practice. Intensity differences between the cameras can be partly compensated by image pre-processing (e.g. by equalization procedures) or using an *ad hoc* Optical Transfer Function (Schanz et al. 2012). It is worth noting that, owing to the expansion of the laser beam in the depth direction and to the relatively large $f_\#$ to achieve properly focused particles, high intensity light sources are needed, and whenever possible large particle sizes.

The seeding concentration is set to achieve a particle image density of 0.05 ppp, which is a typical figure of merit for a successful tomographic reconstruction (Scarano 2013). Tomographic PIV shares with other 3D velocimetry approaches the limit in terms of ambiguity of the reconstruction, i.e. the detection of spurious (ghost) particles. Ghost particles tend to move coherently with the set of true particles (Elsinga et al. 2011), thus contaminating the results and, in particular, the velocity gradients in the reconstructed flow field. The selection of the proper particle image density is therefore a compromise between the need for dense information and the minimization of ghost particles. While for standard dual-frame application (like the one described here) the particle image density is usually in the range 0.04-0.06 ppp, higher particle image densities are manageable if temporal coherence can be exploited. The Motion Tracking Enhancement technique of Novara et al. (2010), which is based on the combined use of images from two or more successive exposures, has been used with concentrations up to 0.2 ppp (Novara & Scarano 2012).

In order to reduce the image background intensity, the images are pre-processed by removing the ensemble minimum of the intensity from each pixel, and then subtracting a sliding minimum over a kernel of 31 x 31 pixels in space and 5 realizations in time to remove the residual background. In general, in Tomographic PIV it is desirable to remove all background information to reduce the dimension of the solution space in the reconstruction problem. Therefore, it is good practice to apply the above-mentioned background subtraction techniques and others, such as intensity thresholding and eigen-background removal (Mendez et al. 2017). An overview on the effects of pre-processing on tomographic reconstruction accuracy can be found in Martins et al. (2015).

An optical calibration between physical and image coordinates is carried out using a dual-plane target translated in the measurement domain. Here the

calibration process is challenging since the swirler is tested also in a "confined" configuration, i.e. enclosed in a methacrylate cylindrical chamber. Due to the need of high precision calibration (error below 0.1 pixels, Elsinga et al. 2006), a correction is needed for the distortion effect induced by the cylinder. This is performed following the volumetric self-calibration (Wieneke 2008). Here the residual mapping error is reduced from 3 pixels to 0.07 pixels.

The illuminated volume of approximately 128 x 128 x 46 mm^3 (thus with an aspect ratio of 0.35 : 1 between depth and in-plane dimensions) is discretized in 18 voxel/mm. The reconstructed volume is slightly larger in the depth direction (2298 x 2298 x 1004 voxels) to ensure that all the imaged particles are captured. This also enables *a posteriori* evaluation of the reconstruction quality via the depth profile of the intensity, i.e. by computing the sum of the intensity of the reconstructed particles at different depths (Scarano 2013). An intensity ratio of 2 between the region inside and outside the volume is typically accepted as a minimum quality check. The reconstruction is performed with a variant of the SMART algorithm (Mishra et al. 1999), which is an iterative algebraic method. The convergence is enhanced calculating the first guess using a Multiplicative Line of Sight approach (MLOS, Atkinson & Soria 2009). Other computationally efficient solutions are the multi-resolution MART reconstruction (Discetti & Astarita 2012a), which refines progressively the voxels resolution during the reconstruction process, or the sequential Motion Tracking Enhancement (Lynch & Scarano 2015) for time-resolved applications. In algebraic reconstruction strategies, it is also common to smooth (e.g., with a Gaussian filter) the reconstructed volumes between each iteration to regularize the solution (Discetti et al. 2013, Castrillo et al 2016).

The 3D particle field motion is computed with a computationally efficient direct sparse cross-correlation approach (Discetti & Astarita 2012b), based on a multi-step volume deformation algorithm (Scarano 2001). The final interrogation spot is of 64 x 64 x 64 voxels, corresponding to 3.6 x 3.6 x 3.6 mm^3, with an overlap of 75%. The uncertainty in the velocity spatial derivatives is estimated computing the standard deviation of the divergence computed on raw data, which results being about 7% of the typical value of the vorticity magnitude within the shear layer.

An example of instantaneous 3D velocity measurement of the swirl injector flow is reported in Figure 4. Velocity vectors along a plane containing the jet axis are shown along with intense vortical structures (identified by the Q criterion of Hunt et al. 1988). The full 3D instantaneous information allows visualizing a helical structure related with the precessing vortex core, characterized by an azimuthally wavy shape due to peaks of radial vorticity. These structures are responsible of the break-up of the helical vortex and its dissipation, which is shown to occur earlier for the confined jet configuration.
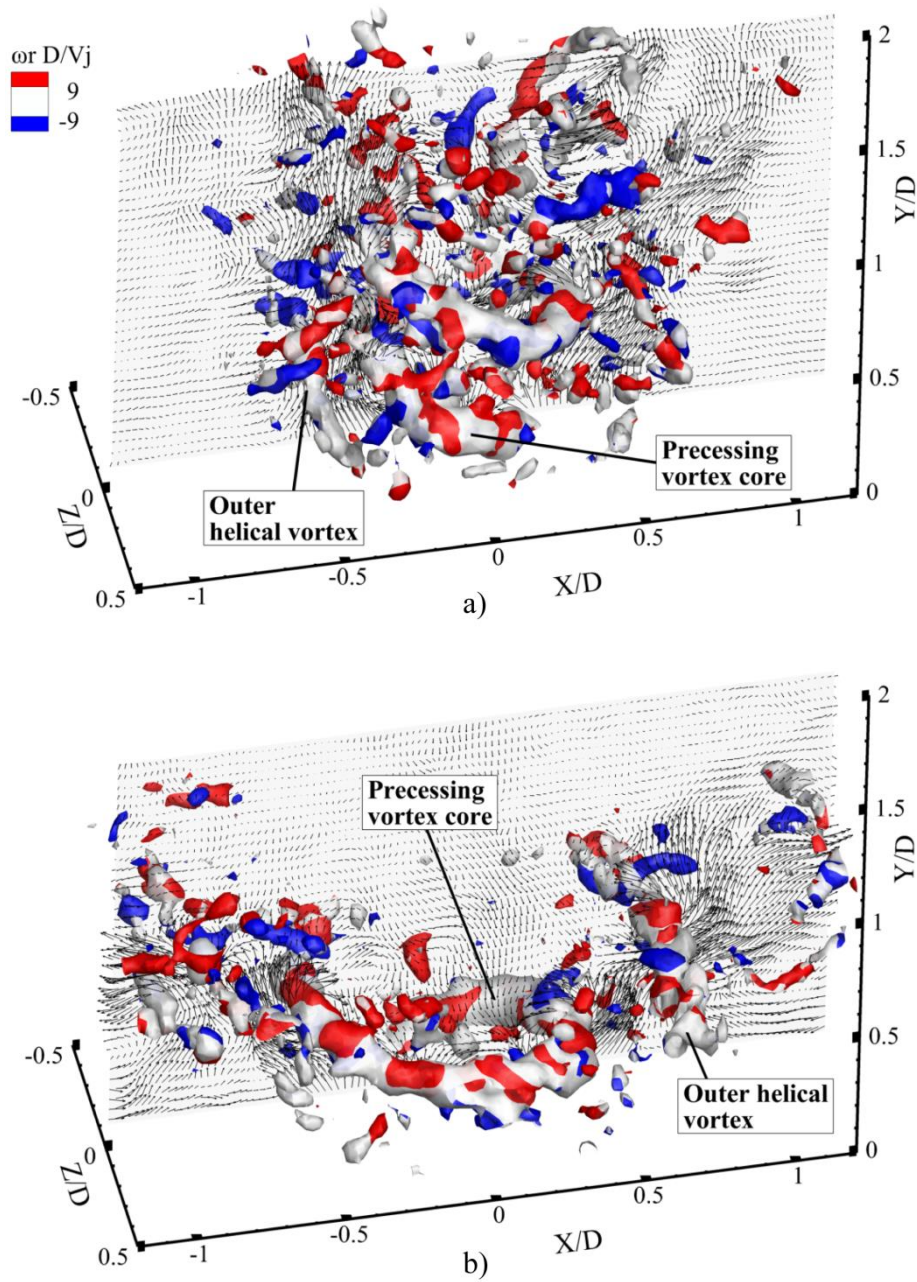
Figure 4 Instantaneous velocity vectors along the symmetry plane of a swirl injector, with vortex cores visualized via the Q criterion, investigated in free (top) and confined (bottom) configuration. Color-coding is based on the normalized radial vorticity. Reprinted from Ceglia 2014, Copyright 2014, with permission from Elsevier.

2.3 Scanning PIV

Scanning light sheet methods extract quasi-simultaneous 3D velocity fields by scanning a volume with a laser sheet (Brücker 1995). In order to obtain a "frozen" representation of the whole flow field, the time to sweep the volume must be much smaller than the characteristic timescale of interest. This, besides requires high-repetition lasers and high-speed cameras, limits the application to low-speed flows. For example, Diez et al (2011) used a 1 kHz laser to perform

11

fine-scale flow measurements in the far field of a turbulent water jet with centerline velocity of 0.020 m/s, and Kolmogorov timescale estimated as 51 ms. This strict requirement can be partly relaxed if the focus is on the large-scale motions.

In its early implementations, scanning PIV included the use of a single camera and standard 2D PIV processing to obtain 3D-2C velocity fields (Brücker 1995). Adding a second camera in stereoscopic arrangement allows the extraction of 3D-3C velocity measurements (e.g., Hori & Sakakibara 2004, Watanabe et al. 2015). The main advantage with respect to full volumetric imaging is the potentially higher spatial resolution. The seeding concentration can indeed be comparable to that of planar PIV, since each recorded image contains only a portion of the particles within the volume, with no 3D reconstruction required. Imaging conditions, however, are in general worse than in planar PIV due to the large $f_\#$ required to obtain well-focused particles throughout the spanned volume.

More recently, a multi-camera version of the method, referred to as Scanning Tomographic PIV, has received some attention (Ponitz et al. 2012, Casey et al. 2013). It consists in using a multi-camera system to reconstruct the 3D distribution of particles/light intensity within thin illuminated slabs scanning through the volume. The advantage with respect to full-volume illumination is related to the limited thickness of the slices, which reduces the ambiguity in the reconstruction (Eq. 2). Casey et al. (2013), for example, used slightly-overlapped 17-25 mm thickness sheets to scan a volume with depth of about 100 mm. The reconstruction of each illuminated sub-volume is performed with a procedure analogous to that of Tomographic PIV. A slightly different implementation is documented by David et al. (2012), in which a single camera is used. The illuminated slabs are much thinner (0.8 mm), and the corresponding images are re-projected in space to reconstruct the 3D distribution of particles, which is then discretized in voxels and interrogated by 3D cross-correlation. A detailed assessment of the method for one and two cameras is reported by Lawson & Dawson (2014) along with a parametric error study.

The Scanning PIV technique in its tomographic implementation is illustrated here via the vortex ring transition study by Sun & Brücker (2017). The experimental setup is sketched in Figure 5. A nozzle fed by a piston-cylinder system is installed in an octagonal water tank and generates vortex rings, whose position with respect to the imaging system is kept stationary by lifting the entire tank at a speed of about 50 mm/s. Imaging is performed by three Phantom V12.1 high-speed CMOS cameras (1200 × 800 pixels) operated at 1250 Hz and positioned at an equal angular spacing of 45°. Similar to Tomographic PIV, a wide angular aperture is needed to reduce the elongation of the reconstructed particles. The objectives are set to $f_\# = 16$ to ensure proper focusing throughout the volume. The illumination is provided by a continuous wave Argon-Ion laser (Coherent Innova 70C, 3 W power), shaped into an 8 mm thick sheet. The volume sweeping is achieved using a rotating drum scanner

with 10 mirrors installed in helical arrangement. The slices are overlapped by 2 mm to ensure continuity of the imaged field, thus reaching a final thickness of 62 mm. A full volume scan is performed at a rate of 125 Hz, which is sufficiently fast compared to the characteristic time scales of the flow under investigation. The flow is seeded with neutrally buoyant particles 60 μm in diameter. Large particles size is needed owing to light intensity limitations when operating with high repetition rate or continuous lasers and to the relatively small lens aperture. The mean particle displacement between successive scans is around 8 pixels.

The result of the reconstruction process is a set of 3D light intensity volumes, discretized with 700 x 519 x 500 voxels at 10 voxel/mm. The velocity fields are then obtained with 3D cross-correlation using an iterative multi-step volume deformation algorithm. A 3D history view of the vortex ring between $10 < t^* < 60$ (where $t^* = \frac{t\Gamma_0}{R^2}$, being Γ_0 the circulation and R the vortex radius) is reported in Figure 6. At $t^* = 10$ the ring has a smooth shape and it is still laminar; at $t^* = 20 - 30$ waves develop which generate axial and radial vorticity components. Secondary vortical structures can be observed at $t^* = 40$, and eventually the ring transitions to turbulence ($t^* > 50$).
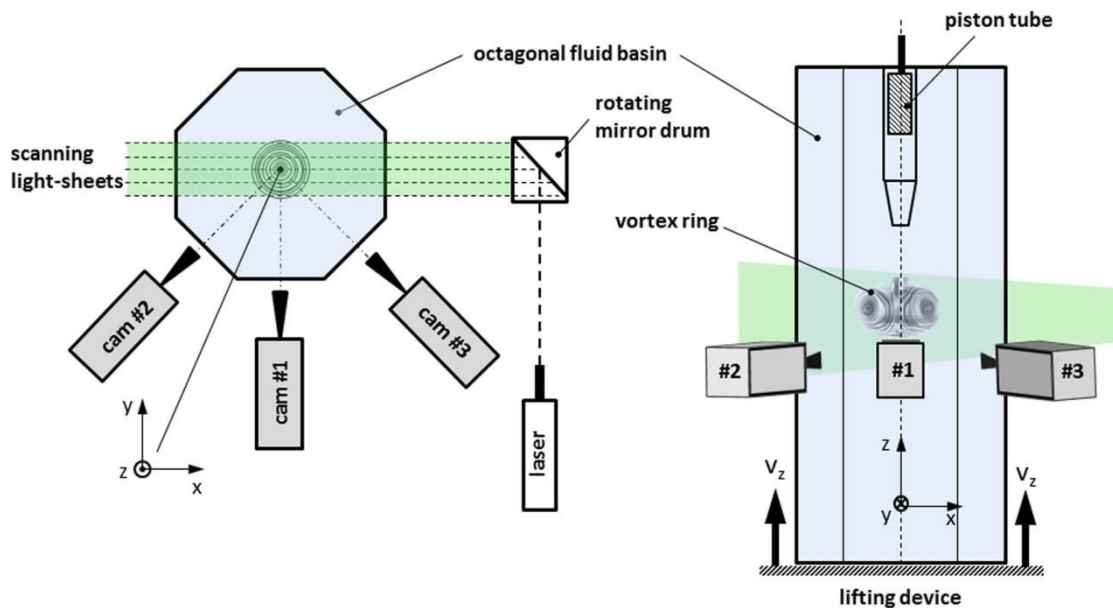

Figure 5 Side view and top view of the Scanning PIV setup used by Sun & Brücker (2017). Figure from Ponitz et al. (2016). Ponitz 2016 © The Visualization Society of Japan 2015. With permission of Springer.
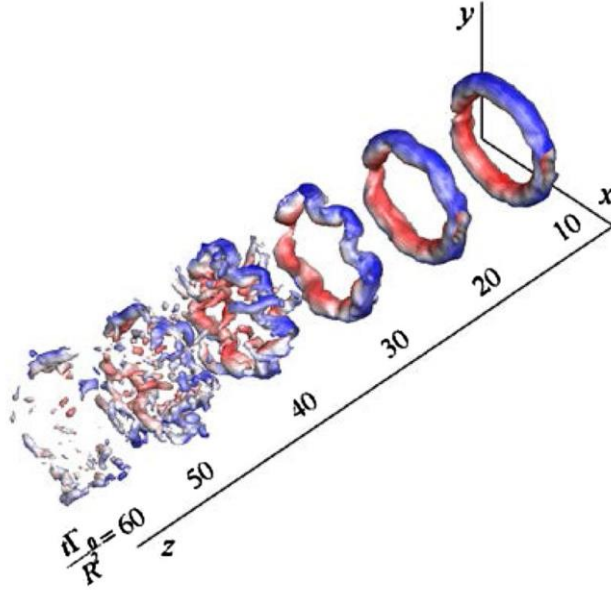
Figure 6 Time history of a vortex ring transition reconstructed by Scanning PIV. The isosurfaces indicate vortical flow identified by the Q criterion and are color-coded with the axial velocity magnitude. Reproduced from Sun 2017. CC BY 4.0.

2.4 Holographic PIV

In holography the amplitude and phase of the light wave scattered by an object is recorded and used to reconstruct the original light field in 3D (Gabor 1948). In velocimetry applications, this is obtained by directing a beam of collimated light (typically a laser) through the field of view seeded with tracer particles (Katz & Sheng 2010). The scattered light is superimposed to a reference beam, generating an interference pattern which is stored on a recording medium to form a hologram. The latter is essentially a 2D image containing (circular) interference patterns for each illuminated (spherical) particle. The particle size is encoded in the low-frequency content of the pattern, while the high-frequencies encode the particle position along the direction normal to the imaging plane. When the developed hologram is illuminated (physically or virtually) with the complex conjugate of the reference beam (i.e., propagating in a direction opposite to the latter), the resulting transmitted light generates a representation of the 3D image of the particles. Image-based cross-correlation is not straightforward due to the nature of the interference pattern (Meng et al. 2004), therefore the velocity field is typically obtained by 3D PTV using the particle coordinates at successive time instances. The data is either investigated in a Lagrangian framework (Gopalan et al. 2008, Lu et al. 2008) or projected on a Cartesian grid (Sheng et al. 2008, Talapatra & Katz 2012).

Holographic systems are typically classified based on whether the reference beam and the object beam are inclined at a finite angle (off-axis) or parallel (in-line). In off-axis configurations, the fringe spacing in the interference pattern is a fraction of the light wavelength, and decreases with increasing angle between the beams. The resolution needed for the recording media is of thousands of

lines per mm, which can only be achieved by specialized photographic films (Hinsch 2002). However, the sensitivity of these supports is low, and high-intensity laser light in forward scattering is needed to image small tracer particles. In in-line configurations, the angle between reference and object beam is constrained to be less than the angle subtended by the plane of imaging, and in many applications both beams coincide. In comparison with off-axis holography, this involves a much simpler optical system and, due to the small angle between the interfering beams, produces relatively large fringe spacing, which can be resolved by digital sensor arrays. Recording digital holograms allows for a large number of fields at high temporal resolution. Furthermore, because of the superior light efficiency of forward scattering, the required laser power is greatly reduced. All these factors have contributed to make Digital In-line Holography (DIH) the most successful implementation of this technique in fluid mechanics. Extremely high spatial resolution can be achieved; for example, Sheng et al. (2008) investigated a turbulent channel flow and obtained vector fields with spacing 51 μm × 136 μm × 17 μm (3 × 8 × 1 wall units) in streamwise, wall-normal and spanwise directions, respectively. DIH is also attractive for the compact and relatively inexpensive set up: a low-power laser, collimating optics, and only one camera.

Some significant disadvantages, however, have limited the diffusion (and commercialization) of holography for volumetric velocimetry. A critical issue, which is particularly severe for in-line systems of small numerical aperture, is the 'depth-of-focus' (DOF), i.e. the longitudinal size of a diffraction-limited point-source image. In forward scattering, this is typically ~ 1 mm for 20 μm particles (Katz & Sheng 2010), severely affecting the accuracy of the reconstructed particle coordinate along the direction normal to the plane of imaging. The problem is partly alleviated when using microscopic imaging, but this in turn limits the measurement volume (typically < 1 cm^3, e.g. Talapatra & Katz 2012). The attainable imaged volume and particle concentration are also limited by the speckle noise due to pattern self-interference from particles along the same optical axis. Finally, the extraction of the 3D particle position (segmentation) is computationally expensive, and has often relied on user-dependent thresholding criteria (Toloui & Hong 2015).

In an effort to overcome these limitations, Toloui et al. (2017) recently demonstrated a novel DIH approach, and we use their test case as a sample application. They investigate the flow above a rough wall in a turbulent channel facility (cross-section of 50 mm × 50 mm). The fluid (NaI aqueous solution at 40% by weight) matches the refractive index of the Polydimethylsiloxane (PDMS) polymer used to manufacture the rough bottom wall, which features 1.5 mm tall tapered pillars (Figure 7). Refractive-index-matching is especially critical in holography due to the potentially large effect of speckle noise on the 3D reconstruction process. The channel is operated at a bulk Reynolds number ≈ 22,770. The imaging setup includes a continuous He-Ne laser, a spatial filter, a collimation lens, and a high-speed camera. The latter is operated at about 3

kHz, and is equipped with a Nikon lens (105 mm focal length, f/2.8G) to obtain a 10 μm/pixel resolution on the streamwise/wall-parallel focusing plane, about 3 mm from the rough wall. The 1472 × 1448 pixel holograms are used to reconstruct a 14.7 mm (streamwise) × 50 mm (wall-normal) × 14.4 mm (spanwise) volume. This is much larger, especially in depth, than typical DIH applications. Moreover, the channel is entirely seeded with silver-coated 8 − 12 μm hollow glass spheres, while often tracer-laden fluid would be locally injected to reduce speckle noise from cross-interference of particles along the light path (Talapatra & Katz 2012). Here the signal-to-noise ratio (SNR) is first enhanced through subtraction of a time-averaged hologram followed by gray-scale equalization. The detectable particle concentration is then increased by iteratively removing particles from the hologram, allowing the identification of particles otherwise hidden by objects in the foreground (Toloui & Hong 2015). For reconstructing the particle positions, the 3D deconvolution method (Latychevskaia et al 2010) is employed, which models the optical field as the convolution of the particle field with a point-spread function based on Rayleigh-Sommerfeld's diffraction theory. This procedure was shown to reduce the particle DOF by ~ 20% - 40% (Toloui & Hong 2015). Other strategies have been proposed to minimize the DOF issue, notably imaging the tracer particles with multiple cameras from different angles (e.g., Soria & Atkinson 2008). This however requires careful alignment and calibration, somewhat hindering the simplicity of the DIH setup. Here, in order to reduce human intervention, 3D particle segmentation from the background is performed with an automatically selected local threshold, obtained by scanning the minimum intensity map with a small interrogation window. To minimize particle misidentification, an iterative predictor-corrector 3D tracking algorithm is used: the displacements are first obtained only from the particles detected as they travel through the entire sampling volume, and these set local bounds for the displacement field in successive iterations. Here this approach allows tracking particles at a concentration of 0.0035 ppp, which is much lower than in Tomographic PIV but still significantly higher than in previous DIH applications. About 7500 tracks are reconstructed for each pair of holograms, allowing for interpolation on an isotropic Cartesian with about 1.1 mm spacing. The velocity component normal to the imaging plane (here the wall-normal component) is the least accurate due to the DOF effect. An attempt to alleviate the problem is made by using the in-plane components and calculate the third one by continuity, with a second-order finite difference scheme for the velocity derivatives. Verification with two orthogonal cameras shows errors up to 16% in the absolute and up to 40% in the fluctuating velocity in wall-normal direction, highlighting the challenges associated with this aspect of DIH.

Figure 8 shows consecutive flow realizations (separated by 20 ms). The streamwise span is extended using Taylor's hypothesis, and coherent vortical structures are visualized by 2D swirling strength (Zhou et al. 1999) in the wall-normal direction. Typical elongated and inclined structures appear to grow

towards the outer layer, and more activity is visible above the bottom rough wall.
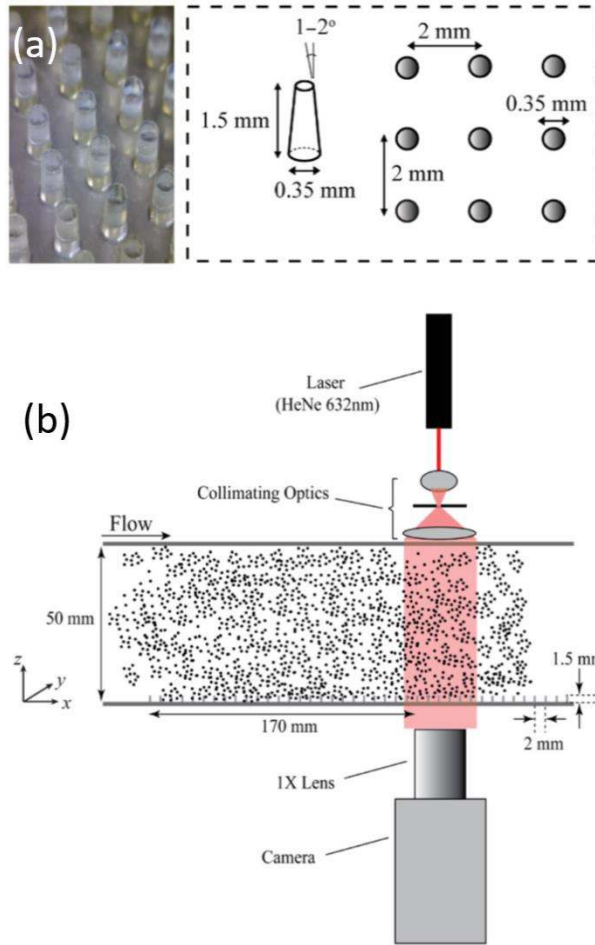
Figure 7 Close-up view and schematic of the PDMS cylindrical elements (a) roughening the bottom wall of a channel studied by DIH, with schematic of the imaging setup in (b). Reproduced from Toloui et al 2017. © IOP Publishing Ltd. All rights reserved.

Figure 8 Sample of consecutive instantaneous fields with contours of streamwise velocity and iso-surfaces of wall-normal swirling strength for the turbulent channel. The upper wall is smooth and the bottom wall is rough. Reproduced from Toloui et al 2017. © IOP Publishing Ltd. All rights reserved.

2.5   Defocusing PIV

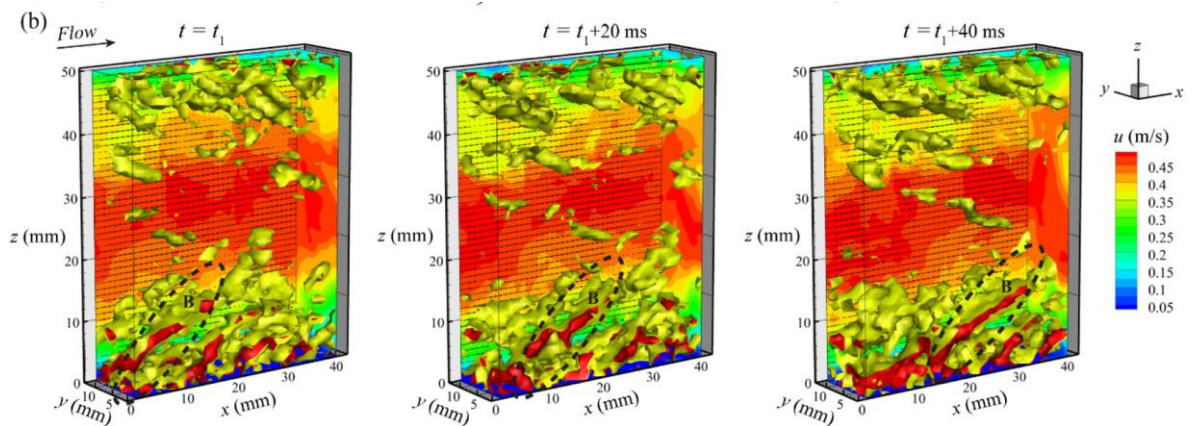The defocusing principle exploits the depth-information encoded in the size/shape of the imaged particles. The main advantage of this technique is that it can be potentially implemented using a single camera, thus allowing its application in facilities with limited optical access. Defocusing Particle Image Velocimetry was proposed first by Willert & Gharib (1992). In its original implementation, a three-pinhole aperture is used instead of the standard single-pinhole aperture. With this optical arrangement, the light scattered by each particle generates three particle images on the camera sensor. The distance between the particle images encodes the depth position, while the orientation of the triangle removes the ambiguity on the position of the particle with respect to the focusing plane. A theoretical formulation of the technique has been proposed first by Pereira et al. (2000) and successively refined by Pereira & Gharib (2002). The proposed model was strictly valid for two-dimensional imaging; subsequent extension to full-3D formulation has been contributed by Kajitani & Dabiri (2005) and then improved by Grothe & Dabiri (2008). The image processing step relies on identifying particles triangles on the images via pattern matching techniques, determine the triangle size with sub-pixel accuracy, and locate the particles in the 3D volume; this operation is repeated for each exposure, and then particle tracking is generally used to determine velocity vectors (Pereira et al 2006).

A different approach of the defocusing principle consists in encoding the depth information using astigmatic or anamorphic imaging. An astigmatic imaging system possesses two distinct focal lines; consequently, point sources are imaged as ellipses. A simple implementation of the technique is obtained by using a cylindrical lens (Kao & Verkman 1994). This optical arrangement results in oblate/prolate particle images, whose aspect ratio and orientation depends on the depth location. After locating the particles in the volume, tracking techniques can be used to extract the 3D-3C velocity field. Clearly, to avoid ambiguity, the particles must be located within the two focal planes. The technique has been demonstrated for macroscopic flows by Angarita-Jaimes et al. (2006) and assessed for microscopic flows by Chen et al (2009). The capability of dealing with limited optical access, and the ease of implementation by simply adding a cylindrical lens, lead to developments particularly in microfluidics. Further improvements of the technique have been provided by the group of UNIBW Munich (Cierpka et al. 2010a, Cierpka et al 2010b), and finally established Astigmatism μPIV as a valid option for 3D-3C microfluidics (Cierpka et al. 2012, Cierpka & Kähler 2012).

As an example of application of Defocusing PIV, the investigation of the wake of a hydrokinetic turbine by Chamorro et al (2013) is considered. The experimental setup is sketched in Figure 5. A miniature 3-blade axial-flow turbine (with rotor diameter d=0.126 m and hub height of 0.11 m) is placed in a recirculating flume facility. The free stream velocity at the hub is U_{hub}=0.2 m/s and the angular velocity is Ω = 14.7 rad/s, thus yielding a tip speed ratio λ =

$\Omega d/2U_{hub}$= 4.65. The resulting Reynolds number based on the hub velocity and rotor diameter is $Re \approx 2.5 \cdot 10^4$. Spherical ceramic particles (65 μm in diameter, density of 0.8 g/cm³) are used to seed the flow; the illumination is provided by a dual-cavity Nd:Yag pulsed laser (200 mJ/pulse). The laser edges are cut with a cover plate to remove the low intensity tails.
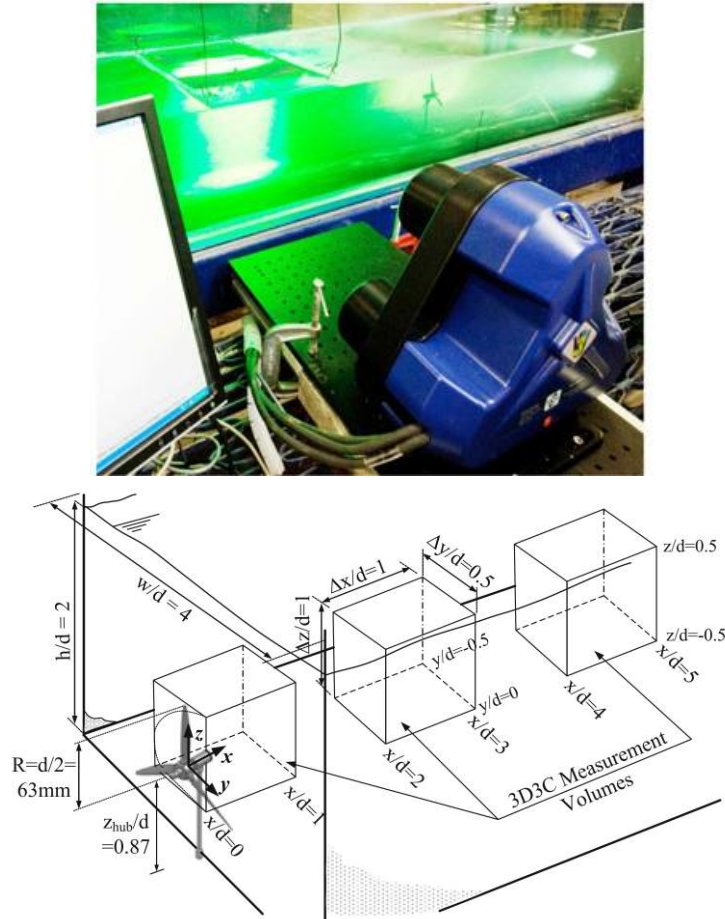

Figure 9 Top: photograph of the experimental setup used by Chamorro et al. (2013) to image the wake of a hydrokinetic turbine by Defocusing PIV. Bottom: sketch of the measurement volumes. Figure from Chamorro et al. (2013). Chamorro 2013 © Springer-Verlag Berlin Heidelberg 2013. With permission of Springer.

Owing to image density issues (each particle results in three particle images) and to possible errors in the determination of the triangular patterns, the allowed particle concentration is rather limited in Defocusing PIV. Chamorro et al. used a 3-sensor arrangement, in which each of the three projections of the particles is recorded on a different sensor. Different optical arrangements have been proposed to overcome this issue: Lin et al. (2008) developed an annular-aperture defocusing; Tsien et al (2008) used CCD colour cameras and placed different colour filters on each pinhole, with subsequent colour-coding of each particle in the triangle. The 3-camera arrangement used here has the advantage of reducing issues related to light intensity (typical of pinhole-based arrangements). Additionally, it allows an increase in the equivalent distance between the pinholes, thus improving the particle depth location accuracy

19

(Pereira & Gharib 2002). The particles are then identified on each sensor, located in 3D, and tracked in two subsequent exposures using a two-frame particle tracking scheme (Pereira et al. 2006). The final observation region is a volume of $120 \times 140 \times 60$ mm³ (Figure 9), with each realization yielding approximately 12000 vectors. The randomly spaced vectors are interpolated on a structured grid with a Gaussian-weighted interpolation based on the distance between the vector locations and the points of the grid. The nodes spacing is set to 2 mm, while the mean distance between vectors in each realization is slightly larger than 4 mm. The absolute spatial uncertainty was estimated using particles glued to a stationary plate located within the measurement volume, i.e. under the same optical conditions as the experiment. This leads to estimates of 4.8 mm/s or 2.5% of the freestream velocity in the wall-normal and streamwise directions, and 4 times larger in the spanwise direction.

The 3D instantaneous distribution of vorticity due to the shedding of tip vortices is reported in Figure 10, with both isosurfaces and contours along two selected slices of the volume. The visualization allows quantification of the spacing between the tip vortices, dictated by the tip speed ratio. The wake growth is also clearly highlighted, depicting a complex flow field with changes of the local convection velocity, also due to the mean shear and the interaction between vortices.

(a)   **(b)**

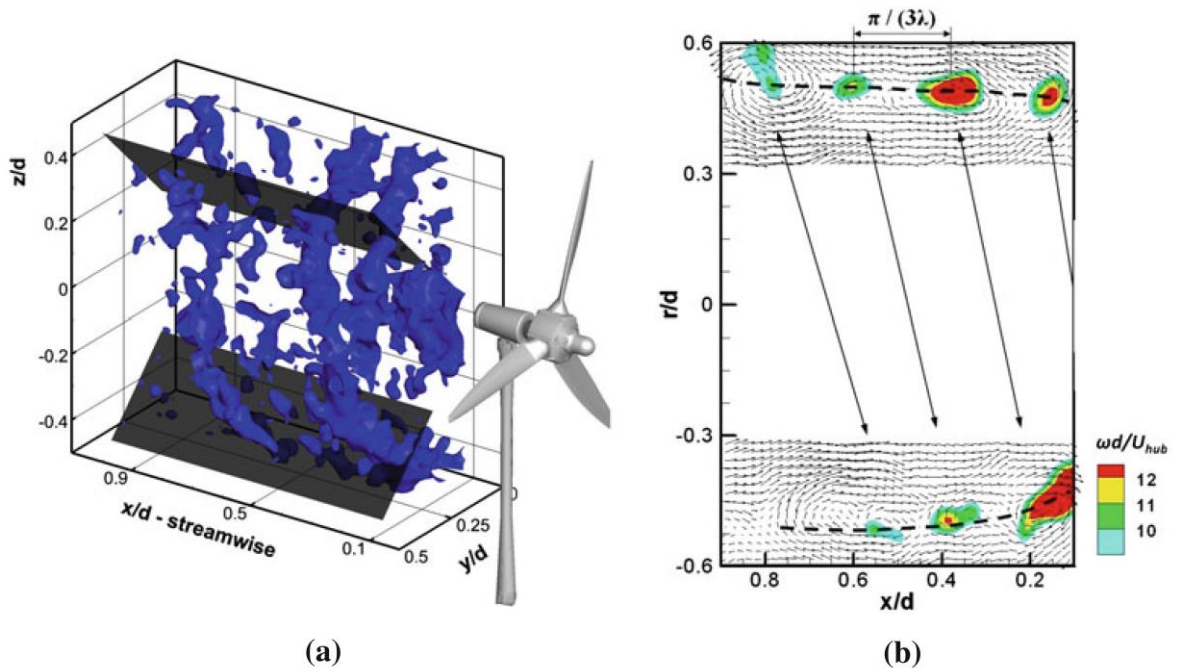Figure 10 Tip vortices in the near-wake of the turbine imaged via Defocusing PIV by Chamorro et al. (2013). Vorticity isosurfaces at $\omega d / U_{hub} = 12$ are shown in (a), while in (b) vorticity contours and vector field are shown along the shaded planes highlighted in (a). Figure from Chamorro et al. (2013). Chamorro 2013 © Springer-Verlag Berlin Heidelberg 2013. With permission of Springer.

2.6 Light-field imaging

Instead of recording the three-dimensional position of tracer particles, an alternative strategy is to reconstruct their light field information. This approach is followed by synthetic aperture PIV (SAPIV, Belden et al. 2010), which leverages synthetic aperture refocusing: an array of multiple cameras, looking at the same scene from slightly different viewpoints, simulates a lens of an arbitrary sized aperture (Vaish et al. 2005). This is used to capture the light field, i.e. the complete distribution of light in space. The latter can be described by the five-dimensional plenoptic function (Adelson & Bergen 1991), where each ray is parameterized by its position (three spatial coordinates) and direction of propagation (two angles). In a transparent medium the radiance remains constant along each light ray, reducing the light field to a 4D function (Levoy 2006). To reconstruct the particle light field, images from all cameras are projected onto a focal surface in the scene, and recombined to yield a synthetic image. This process is repeated for an arbitrary number of focal planes, simulating a camera system with a narrow depth-of-field scanning through the light field. Particles away from the focal plane appear significantly blurred and can be removed by thresholding. The refocused images at various depths are stacked to build a 3D intensity volume, and standard cross-correlation procedures are used to determine the 3D-3C displacements. For sufficient separation between the centers of projection of the sensors in the array, some of the cameras can see particles which are occluded to others, producing a "see-through" effect. This can be very beneficial in optically dense environments such as bubbly flows (Belden et al. 2012), or to image the flow around objects (Langley et al. 2014).

Instead of using multiple cameras, another route to light field imaging is to use a plenoptic camera, i.e. a single sensor capable of measuring both position and angle of the light rays (Adelson & Wang 1992). In this device the main imaging lens focuses the entire angular distribution of light onto an array of microlenses, each covering a small number of pixels on the sensor. The microlenses capture the spatial information contained in the light field, while the pixels contained under the microlens record the angular distribution. This concept has been recently applied to obtain 3D PIV measurements (Fahringer et al. 2015, Shi et al. 2017), and enables volumetric imaging in applications with limited optical access and using a compact hardware setup. This promising approach is still in its infancy. While thus far the technique has been demonstrated using plenoptic cameras built in-house, recently commercial models have appeared.

To illustrate important aspects of volumetric velocimetry based on light-field imaging, we consider the study by Mendelson & Techet (2015) who use SAPIV to investigate the 3D flow around (and the body kinematics of) a freely swimming fish. Experiments are conducted in a five-gallon tank filled up to a level of 160 mm, with the fish constrained to swim in the center portion of the tank. Illumination is provided by a 1000 W, 808 nm laser operated with a pulse

duration of 50 µs. Near-infrared light is an effective solution to image animals that respond to visible light (Adhikari & Longmire 2012a). To counteract the strong light attenuation in water, a surface mirror is placed at the end of the tank to reflect the beam back into the volume. The camera array consists of nine 1.2 MP CCD cameras (Manta, Allied Vision Technologies) operated at 30 Hz, and is positioned to view through the side of the tank (Figure 11). The large number of cameras needed to reconstruct the light field is a signature feature of SAPIV. The parametric study of Belden et al. (2010) suggested an optimum between 10 and 13 cameras, which does increase the setup optomechanical complexity. On the other hand, high-quality scientific sensors are not necessary because the averaging process in the reconstruction effectively reduces the impact of camera noise; therefore lower-cost computer vision cameras can be used. Here each camera is equipped with a 35 mm Tamron lens set to $f_\# = 5.6$. Similar to other 3D optical imaging techniques, relatively high numerical aperture is required to keep the entire measurement volume (here $70 \times 60 \times 40$ mm^3) in focus. The achievable seeding density in SAPIV is affected by the depth elongation of the volume, similarly to Tomographic PIV, LPT and Defocusing PIV. In this case the tank is seeded with 50 µm polyamide tracers to a density of 230 particles/cm^3, resulting in an image density of 0.03 ppp. According to the simulations of Belden et al. (2010), SAPIV can handle higher particle densities (up to 0.09 ppp for a (50 mm)^3 imaged volume), although significantly lower concentrations have been demonstrated in experiments. For better reconstruction the particle images are artificially enlarged by convolving the raw images with a 3×3 pixel Gaussian kernel. As in other 3D PIV methods, the reconstruction is sensitive to background light and its distribution. Here spatial normalization is performed with a local min/max filter (10×10 pixel window). A sliding minimum is then subtracted to counteract possible background amplification caused by the normalization.
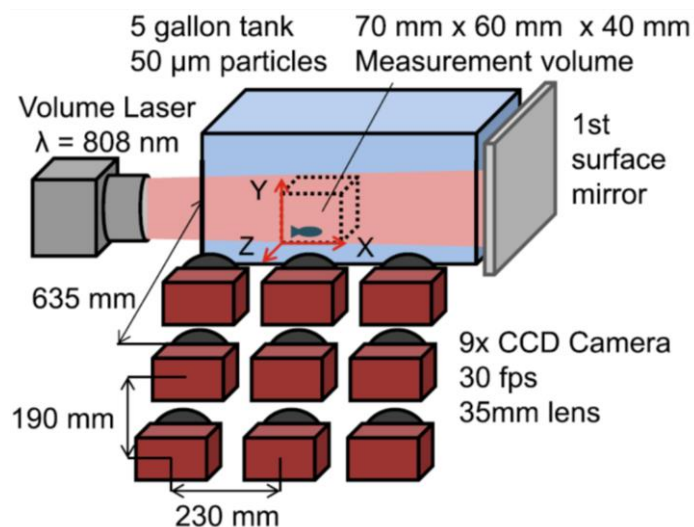

Figure 11 Experiment setup for SAPIV measurements of a swimming fish. From Mendelson & Techet (2015). Mendelson 2015 © Springer-Verlag Berlin Heidelberg 2015. With permission of Springer.

The camera array is positioned 635 mm from the tank in a 3 × 3 arrangement with 230 mm horizontal and 190 mm vertical spacing. The camera spacing and the distance from the front of the imaged volume determine the resolution in the depth direction, which is a linear function of the depth (Belden et al. 2010) and here is about 0.2 mm.

The synthetic aperture refocusing process formalized by Belden et al. (2010) is based on the map-shift-average algorithm, in which the transformation for the various focal planes is reduced to a linear coordinate shift. In the present case (as in most PIV/PTV experiments), refractive interfaces are present and thus refractive SA refocusing is needed (Belden 2013). The camera array is mapped using a calibration procedure that compensates for refractive effects, which involves traversing and imaging a calibration plate through the investigated volume. The reconstruction becomes computationally intensive because back-projection through refractive interfaces involves an iterative step for each pixel to ensure Snell's law is satisfied for each ray. Bajpayee & Techet (2017) recently proposed an alternative approach based on a highly parallelizable fit algorithm, applicable if all refractive interfaces are planar.

In SAPIV the image recombination in the refocusing process can be additive (Belden et al. 2010, Langley et al. 2014) or multiplicative (Belden et al. 2012). The latter is essentially analogous to line-of-sight reconstruction techniques used in Tomographic PIV (Atkinson & Soria 2009, Maas et al. 2009), and enhances the SNR of the refocused images. However, it requires successful imaging of the particles by all cameras. Here the fish body hides important regions in its vicinity, and the additive method is adopted. The final interrogation window size of the 3D cross-correlation is 64 × 64 × 16 pixels in X, Y, and Z directions, respectively (see Figure 11). The interrogation volume is sized such that the three dimensions are of similar physical size. With a 50% overlap the final vector spacing is 1.85 mm in X and Y and 1.60 mm in Z.

Swimming kinematics are evaluated by tracking reference points on the fish body such as eyes, fin-body junction, and tips of the caudal fin. Masking of the fish is performed using the visual hull method (Adhikari & Longmire 2012b). Compared to Tomographic PIV applications (e.g., Murphy et al. 2013, Adhikari et al. 2016), the visual hull reconstruction in SAPIV benefits from the large number of views, reducing the overestimation of the body volume. This is especially important when imaging slender features such as fins or wings, as also shown in the free-flying butterfly measurements of Langley et al. (2014).

Figure 12 shows velocity and vorticity fields from two perspectives at three time steps during and after a turn executed by the fish. The thrust jet and vortex ring coming off the caudal fin can be clearly identified, along with the motion of the caudal fin indicated by the trajectory of its two tips.
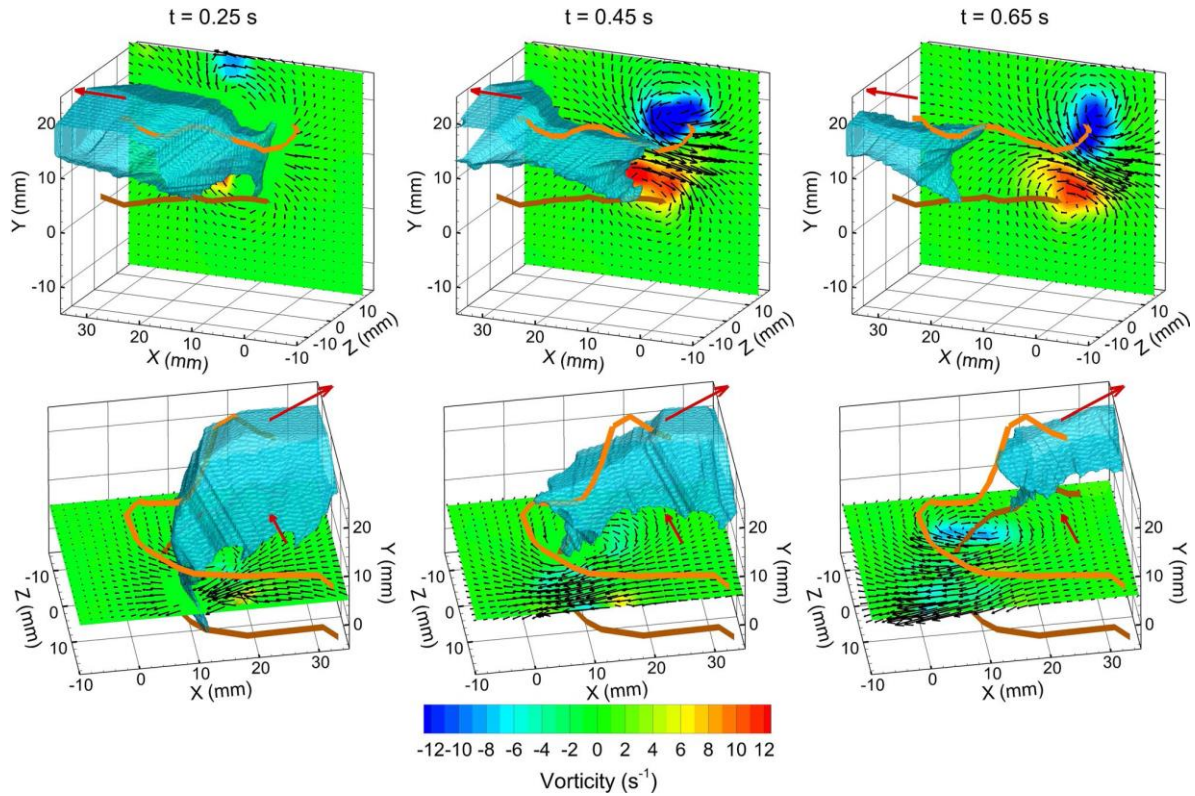
Figure 12 Wake during and after a 75° turn executed by a freely swimming fish imaged by SAPIV. Both rows show different viewpoints. Slices extracted from the imaged volume through the caudal fin and below the fish body (cyan hull) show vorticity contours and in-plane velocity vectors. The solid orange traces are the path of the two caudal fin tips. From Mendelson & Techet (2015). Mendelson 2015 © Springer-Verlag Berlin Heidelberg 2015. With permission of Springer.

2.7   Magnetic Resonance Velocimetry

Magnetic Resonance Velocimetry (MRV) is an application of Magnetic Resonance Imaging (MRI). MRI allows the spatial reconstruction of an object by manipulating nuclear "spins" exhibited by atoms with an odd number of protons or neutrons. A constant magnetic field causes the spins to align with it while precessing at a frequency proportional to the field strength. The spins are then perturbed away from the alignment direction by the application of radio frequency (RF) pulses. After each RF excitation, the spins return to equilibrium emitting a complex electromagnetic signal which is the Fourier transform of their density distribution, and is acquired by a coil surrounding the object under investigation. Spatial localization is obtained applying linear magnetic field gradients along the three spatial directions, with spins at different locations contributing different frequencies to the signal. The gradients are applied sequentially and the excitation/acquisition cycle is repeated. A row of the 3D data matrix in Fourier space is generated at each repetition, and a Fourier anti-transformation returns the volumetric image in physical space.

When imaging fluid flows, quantitative assessment of local velocity can be obtained from the phase shift in the MR signal created by the spin motion along a magnetic field gradient. However, since MRI reconstruction is carried out in Fourier space, the acquired velocity field is usually not a "snapshot". Based on

the desired resolution, a potentially large number of sequence repetitions are needed to fill the data matrix in Fourier space. Moreover, one velocity component is measured per sequence execution. The acquisition time is ultimately proportional to the number of voxels, and for 3D-3C velocimetry it may amount to several tens of minutes. Therefore, the measured velocity field is either the temporal average of a steady flow or a phase-locked average of a periodic flow. Even though instantaneous measurements are not achievable, Reynolds stresses can be estimated leveraging turbulent de-phasing, i.e. the signal attenuation due to random motions in turbulent flows (Elkins et al. 2009). In most fluid mechanics applications the working fluid is water, often doped with contrast agents which increase the rate at which the magnetization returns to equilibrium, increasing the signal intensity. The method described above, often referred to as phase-contrast MRI, is the most commonly used in fluid mechanics applications. Other methods include spin-tagging, which involves tracking a material volume of fluid to estimate its velocity via a time-of-flight approach. For details on MRI-based velocimetry, the reader is referred to reviews from Pelc et al. (1994), Fukushima (1999), Elkins & Alley (2007) and Markl et al. (2012).

MRV allows the measurement of volumetric, three-component velocity fields without the need for optical access, and is therefore well suited to investigate internal flows in complex geometries in biomedical settings. As an example, we consider the study of the pulsatile flow in a model of giant cerebral aneurysm recently carried out by Amili et al. (2017). The aneurysm geometry (Figure 13) was first investigated by Cebral et al. (2011) and later used in the ASME 2012 CFD challenge (Steinman et al. 2013). The inlet vessel diameter is approximately 5.6 mm, and the maximum dimension in the aneurysm sac is approximately 26 mm. To increase the relative spatial resolution, the original geometry is scaled up by a factor of 2.0. The model is manufactured by 3D printing with a wall thickness of 3 mm. High resolution stereo-lithography with 25 μm layers of WaterShed (a resin often used in additive manufacturing) guarantees hydro-dynamically smooth walls. The physiological Reynolds number (Re) and Womersley number (Wo) are matched by adjusting the flow velocity, fluid viscosity, and waveform period. Beside spatial resolution, the increase in physical dimension has the additional advantage of extending (for a given Wo) the duration of the waveform period, which for this *in vitro* experiment is 7.9 s (compared to the *in vivo* period of 1 s). This significantly relaxes the constraint on the temporal resolution of the cycle. The patient-specific waveform is imposed by a computer-controlled cardiac pump, and a combination of flow resistors and capacitance module in the flow loop mimics the impedance of the arterial bed through the standard windkessel boundary conditions (Westerhof et al. 2009). The working fluid is a mixture of water with 25% of glycerine by weight, doped with 0.06 mol/L of copper sulfate to increase contrast. The low copper sulfate concentration does not to appreciably alter the properties of the mixture, see Benson (2011). Other contrast agents such as

Gadolinium can be used (Elkins et al. 2009), but are more expensive. The addition of glycerine has the purpose of enhancing the fluid viscosity (about 2 cSt in the present experiment) and so increase the flow rate at a given Re, resulting in velocities well above the noise floor (about 5 mm/s for standard MRV parameters). However, glycerine reduces the signal intensity and therefore concentrations above 50% are to be avoided. To avoid interference with the strong magnetic field, all parts of the test section and the flow loop in the vicinity of the magnet are non-ferromagnetic. The plastic tubes through which the fluid circulates run through waveguides communicating with an adjacent control room, where the pump, flowmeter and other ferromagnetic components are housed.
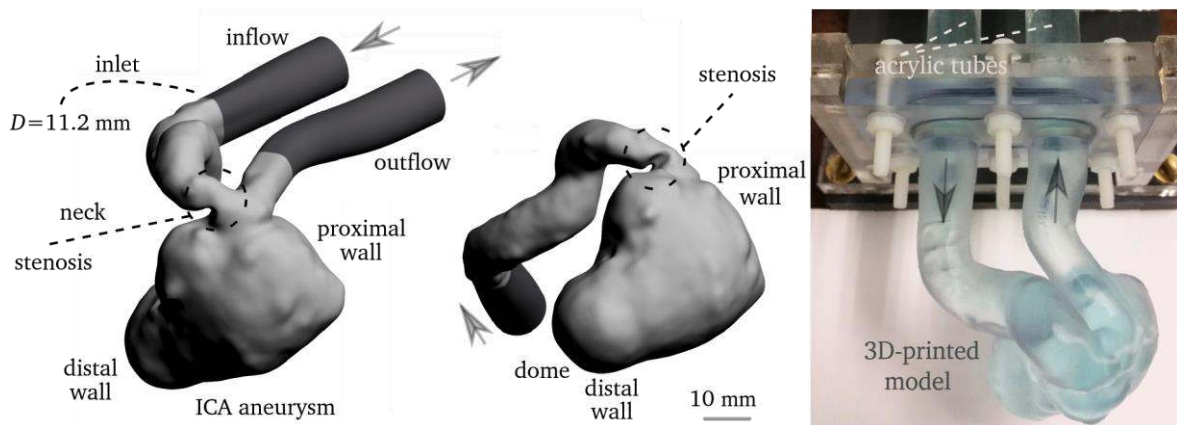

Figure 13 Geometry of the giant aneurysm (left), and 3D-printed scaled-up model filled with water-glycerol mixture infused with copper sulfate (right). The arrows indicate the flow direction. From Amili et al. (2017). Reproduced with permission from Amili.

The measurements are performed using a 3 Tesla Siemens MRI scanner with a head/neck receiver coil normally used to image the human head. Here the spatial resolution is $0.6\times0.6\times0.6$ mm^3 over a field of view $230\times71\times76$ mm^3. The signal increases linearly with the volume of the voxels, and therefore this is a trade-off to obtain sufficiently high resolution without excessively penalizing the accuracy. 3 T scanners are the present standard in MRV studies, due to the balance between high signal (that increases with magnetic field strength) and field homogeneity. 7 T scanners can provide higher resolution (e.g., Cherry et al. 2008 obtained 0.4 mm in all directions), but distortions might arise that need to be corrected for. Phase-locked volumetric flow fields are acquired for 16 segments of the cardiac cycle using the sequence from Markl et al. (2012). To reconstruct the temporal evolution of the flow field, different parts of the Fourier-space data matrix are sampled in different acquisitions corresponding to each phase, and are afterward recomposed in physical space-time, as described in Markl et al. (2003). In order to synchronize the measurements with the waveform phases, the signal from the cardiac pump is used to gate the MRI acquisition. This approach allows reconstructing also flows for which the period is not known *a priori*, although this requires advanced triggering strategies (Wassermann et al. 2013). In principle, the total measurement time increases

linearly with the number of acquired phases, but this can be reduced using parallel acquisition techniques such as the Generalized Autocalibrated Partially Parallel Acquisition (GRAPPA, Griswold et al. 2002). This is used in the considered experiment, and the total scan time is approximately 2.5 hours corresponding to 560 cardiac cycles.

The uncertainty is estimated according to Pelc et al. (1994) and is approximately 7% of the cycle-averaged bulk velocity at the inlet, U_{in}. The main factor in this estimate is the SNR, defined as the ratio of the mean MR signal inside the flow region to the standard deviation of the MR signal outside of it. The SNR increases by a factor $\sqrt{N}$ when averaging N scans (Haacke et al. 1991). In this case two scans are averaged leading to a final SNR of approximately 80. Other methods to estimate the uncertainty have recently been proposed by Bruschewski et al. (2016) and their value needs to be appreciated in the future. Also, the accuracy typically decreases adjacent to the wall due to the possibility that a voxel intersects the solid boundary (*partial volume effect*). This is especially problematic in studies that aim to evaluate, even qualitatively, the wall shear stress distribution, which is a key factor for example in cardiovascular biomechanics. An important step is to carefully mask the flow volume. Here the wall position is determined using an SNR threshold of 8.5, in line with the common choice of using a value one order of magnitude lower than in the fluid region (e.g., Coletti et al. 2014). The reconstructed wall surface is dilated and eroded by one voxel to remove potential artefacts at the boundaries.

In order to eliminate systematic spatial variations in the velocity field due to an imperfect coil response, flow-off scans (with the fluid at rest) are performed with identical acquisition parameters as in the flow-on scans. A polynomial regression is used to fit each velocity component measured during flow-off, and is subtracted from the flow-on velocity field at each phase (Jalal et al. 2016). For these measurements, the flow-off velocity is everywhere less than 1% of U_{in}. An outlier detection method inspired by Westerweel & Scarano (2005) is applied to the velocity field at each phase. This version of the method is based on the local median of the velocity and uses a varying threshold which is function of the local MR signal. Rejected vectors are then replaced with the median of the neighbouring vectors. In addition, a standard 3×3×3 median filter is applied, followed by a solenoidal filter to ensure local continuity (Schiavazzi et al. 2014). Altogether, these filtering techniques produce changes smaller than 10% of the unfiltered data at all points in the flow volume. This post-treatment steps are especially useful to evaluate derived quantities, and in particular: the pressure field, which in this case is obtained by integrating the Poisson equation (Schiavazzi et al. 2017); and the wall shear stress, which is obtained from the dot product of the vorticity vector adjacent to the wall and the local wall-normal vector. For considerations on the accuracy of these quantities for the present data set, see Amili et al. (2017).

Figure 14 illustrates the evolution of the flow pattern in the aneurysm sac, depicting the isosurface of velocity magnitude at a threshold level of $1.5 \cdot U_{in}$,

along with the corresponding streamlines for five cardiac phases. The streamlines show an helicoidal flow at the inlet due to the curvature of the parent artery. The stenosis before the aneurysm neck accelerates the flow before entering the aneurysm sac. The resulting jet reaches the apex of the aneurysm dome, impinges on the distal wall and rolls up. A large vortical structure is present in the sac during the entire duration of the cardiac cycle, and appears more intense at the diastolic and systolic peaks.
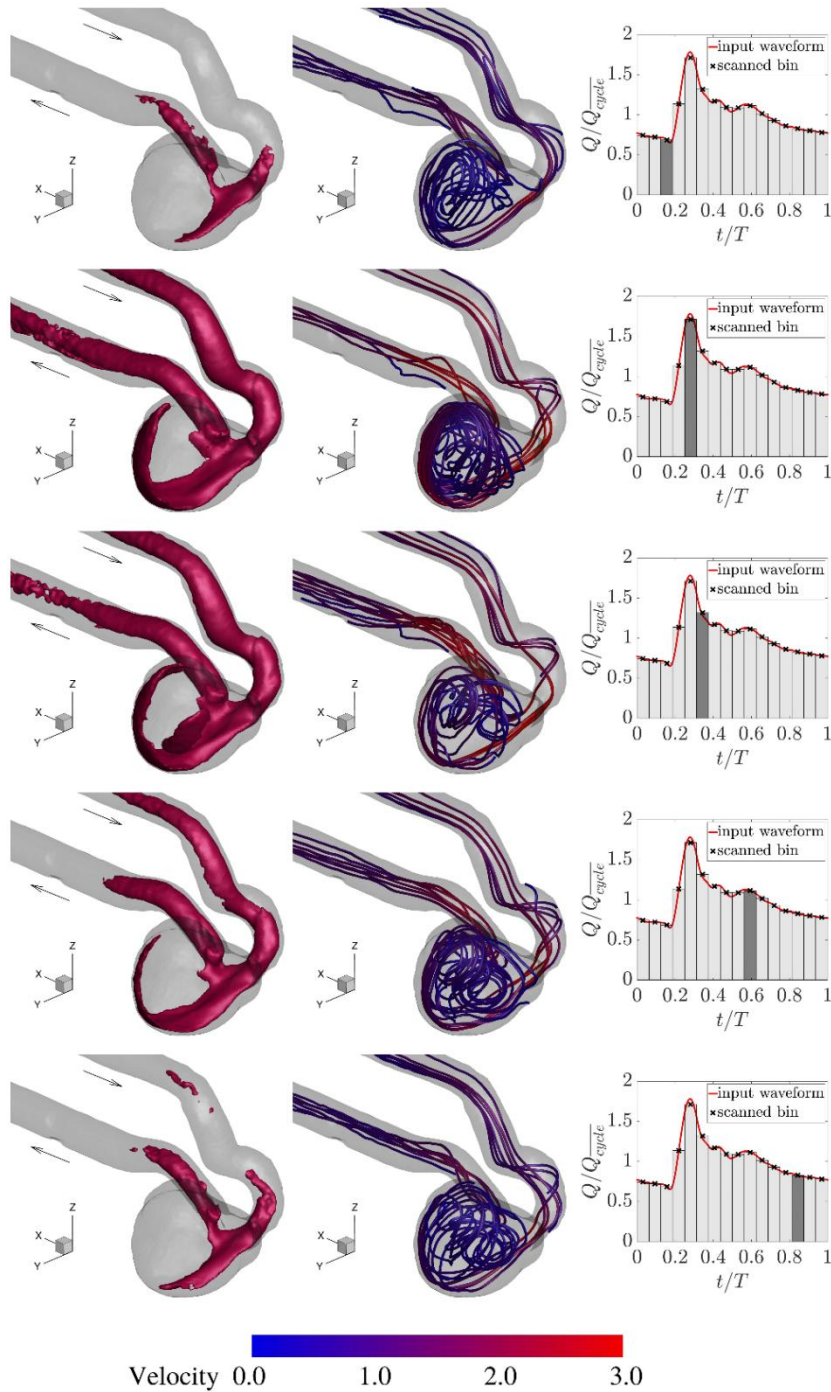

Figure 14 Pulsatile flow field measured by MRV in a giant intracranial aneurysm. Isosurfaces of high velocity magnitude (left) and streamlines colored by velocity magnitude (middle) for different phases of the cardiac cycle (indicated on the right). Adapted by Amili et al. (2017). Reproduced with permission from Amili.

28

3. Discussion

3.1 Classification of optical 3D techniques: reconstruction and motion analysis

As evident from the previous section, the majority of the 3D techniques used by the fluid mechanics community are based on optical imaging of tracer particles. For such methods, the velocimetry follows two distinct steps: (i) the reconstruction of the scene, and (ii) its motion analysis. Based on the first step and considering only full-volume illumination, we can distinguish between:

- Particles-based reconstruction: the extraction of the 3D information is feature-oriented, i.e. it involves the detection and localization (and sometime sizing) of individual tracer particles. Lagrangian Particle Tracking and Defocusing PIV fit in this category.

- Light-field-based reconstruction: the light field distribution is reconstructed using the light propagation direction (Light-field PIV), phase information (Holographic PIV), or intensity back-projection (Tomographic PIV).

The distinction between the different approaches for the velocity extraction is much blurrier. In several cases, the same reconstructed 3D field can be used either to extract Eulerian velocities over a grid (e.g. by cross-correlation), or to follow Lagrangian trajectories. For example, Soria & Atkinson (2008) proposed to measure reconstructed fields from Holographic PIV recordings, but interrogating them via 3D cross-correlation as in Tomographic PIV. Similarly, the Tomographic PTV approach by Novara & Scarano (2013) included a reconstruction based on back-projection as in Tomographic PIV, but evaluated the velocity by tracking particle locations as in LPT. Hybridization is an increasingly diffused trend in volumetric velocimetry, motivated by the need of maximizing accuracy and resolution in different situations, and by the wish of combining advantages from different approaches.

The accurate reconstruction is, of course, a prerequisite for the successful motion analysis. In particle-based methods, there is a limit to the maximum concentration of tracers that can be imaged and reconstructed without ambiguity. In turn, this poses a limit to the achievable spatial resolution in the motion analysis – a constraint which is much stronger in volumetric than in planar velocimetry. The prevalence of 2D PIV over 2D PTV in the last decades is rooted in the robustness of the cross-correlation operator applied to relatively dense particle fields, as compared to pairing of individual particle images in sparse fields. In 3D imaging, on the other hand, a Lagrangian approach can take full advantage of the temporal information, since most tracers remain in the reconstructed volume through successive time steps, thus enabling predictor-corrector schemes. Indeed, the latest developments indicate that the highest

performance is obtained by 3D tracking applied to tomographic recordings (Schanz et al. 2016, Schneiders & Scarano 2016). We elaborate on the techniques' performance in the next subsection. In general, it seems plausible that in the future the distinction among techniques will remain clear only in terms of reconstruction approach; the motion analysis seems increasingly oriented towards Lagrangian frameworks, at least for particle-based techniques that admit time-resolved implementation.

3.2   Dynamic Spatial Range

The Dynamic Spatial Range (*DSR*) defines the achievable spatial resolution for a given measurement domain and, along with the accuracy, is the prime metric of velocimetry performance. In PIV/PTV, the *DSR* is classically defined as the ratio between the linear dimension of the field of view and the maximum allowable particle displacement (Adrian 1997, Westerweel et al. 2013). Here we follow Kähler et al. (2012a) and use an essentially analogous definition (also suggested by Raffel et al. 2007):

$$DSR = \frac{D}{d} \qquad (3)$$

where D is the largest measurable scale (of the order of the largest side of the measurement volume), and d is the smallest resolved scale. This allows us to extend the definition to all considered techniques: d will be the interrogation spot size in cross-correlation algorithms, a function of the average inter-particle distance in tracking algorithms, or the spacing of the 3D data matrix in MRI. Still, the following considerations are primary applicable to particle-based approaches that provide instantaneous realizations (although extensions to ensemble-averaged measurements are later discussed). We note that Eq. (3) represents a best-case scenario, as it assumes measurement noise mostly limited to scales smaller than the resolved ones (e.g., the interrogation window for PIV); in practice, the cut-off length scale is typically larger (Foucaut et al. 2004, Atkinson et al. 2014).

When designing a volumetric measurement, the experimentalist can choose the values of a relatively small set of parameters, each impacting significantly the final resolution: the measurement volume size $\Delta x_0 \times \Delta y_0 \times \Delta z_0$ (z indicating the depth coordinate); the imaging resolution (expressed in pixels per unit length, through the magnification M_0 and pixel pitch d_p); the particle concentration $C = N_p/(\Delta x_0 \Delta y_0 \Delta z_0)$, N_p being the total number of particles imaged in the volume; and the size of the imaging sensor $L_X \times L_Y$ (of course dictated by the available technology). Observing that some of these parameters are not independent (e.g., L_Y/L_X depends on $\Delta x_0/\Delta y_0$ through the sensor resolution), on dimensional grounds we define three main parameters groups: the number of particles N_I contained in a cube of side d; the aspect ratio of the imaging volume $AR = \Delta x_0/\Delta z_0$ (assuming, without loss of generality, that Δx_0

and Δz_0 are the largest and smallest dimensions, respectively); and $DSR = D/d$. Let us now derive an operative expression for DSR as a function of N_I and AR.

Assuming a volume discretization with unit ratio between the size of the pixel projection and the voxel element, the volume size in voxels is $[\Delta x_0 \times \Delta y_0 \times \Delta z_0] \cdot \left(\frac{M_0}{d_p}\right)^3 = [\Delta X_0 \times \Delta Y_0 \times \Delta Z_0]$. Suppose for simplicity the volume has a square cross-section, i.e. $\Delta X_0 = \Delta Y_0 = L$, which is also the linear dimension of the camera sensor (also supposed square, $L_X = L_Y = L$) expressed in pixels. The particles concentration can be related to the image density through:

$$C = \frac{N_p}{\Delta x_0 \Delta y_0 \Delta z_0} = \frac{N_p}{\Delta X_0 \Delta Y_0 \Delta z_0} \frac{M_0^2}{d_p^2} = N_{ppp} \frac{M_0^2}{\Delta z_0 d_p^2} \tag{4}$$

N_{ppp} being the particle image density in particles per pixel. Taking d as the interrogation spot size (for cross-correlation approaches), we can write:

$$d = \sqrt[3]{\frac{N_I}{C}} \tag{5}$$

Considering that the maximum linear extension of the measurement volume is $D = l/M_0$ (with $l = d_p L$ being the physical size of the sensor), by substituting Eq. (4) and Eq. (5) in Eq. (3) we have:

$$DSR = \frac{d_p L}{M_0} \sqrt[3]{\frac{N_{ppp} M_0^2}{N_I \Delta z_0 d_p^2}} = \sqrt[3]{\frac{N_{ppp} d_p L^3}{N_I \Delta z_0 M_0}} = \sqrt[3]{\frac{N_{ppp} L^2 AR}{N_I}} \tag{6}$$

$N_{ppp} L^2$ is simply the total number of particles detected by the sensor. This is related to the number of reconstructed particles, but a univocal correspondence is prevented by both undetected and ghost particles. These can be a significant fraction of the total depending on the technique and experimental conditions (although latest developments indicate dramatic improvements, see Kähler et al. 2016, Schanz et al. 2016). Therefore, we have left N_{ppp} and N_I as independent parameters. N_I plays the role of a parameter related to the desired robustness of the 3D cross-correlation, although the expression is applicable also to particle-tracking: for example, taking d as twice the mean inter-particle distance is equivalent to setting $N_I = 8$ (close to the lower limit for reliable 3D cross-correlation). Equation (6) underlines, for optical techniques, the decrease in effective resolution as the volume aspect ratio approaches unity. A low AR (i.e., a comparable extension of the volume in all directions) is an important factor to capture truly three-dimensional flows, although thin volumes may be sufficient to describe flows with at least one statistically homogeneous direction. In Figure 15 the DSR of several volumetric velocimetry studies (listed in Table 1) is

compared with Eq. (6). The latter is shown to capture the trend, and may be used as a practical estimate in the experiment design phase.
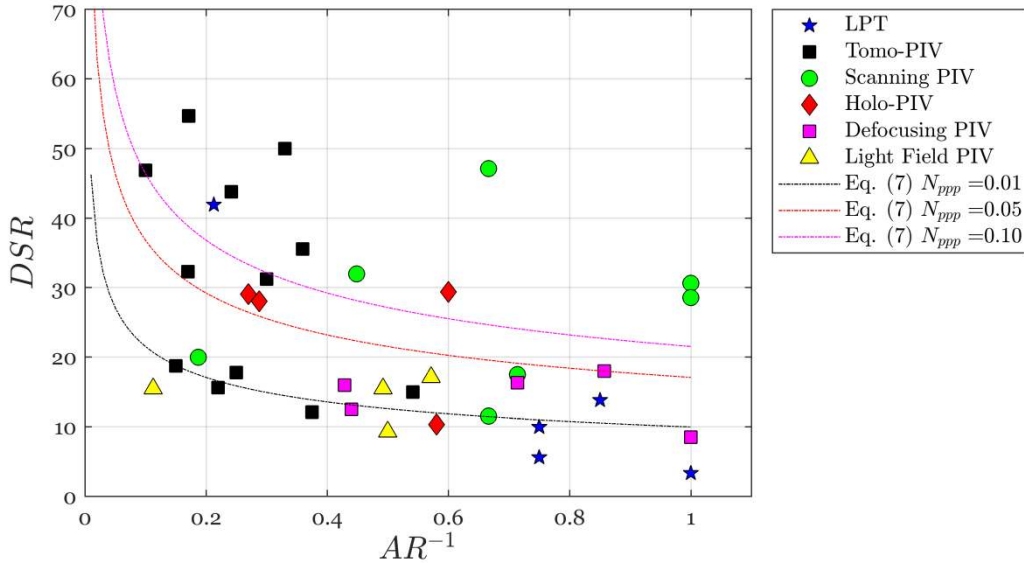

Figure 15 Dynamic Spatial Range and inverse volume aspect ratio for the applications reported in Table 1. The DSR estimated via Eq. (6) is shown (lines), assuming $N_I = 10$ and $L = 10^3$ pixels, and for different values of N_{ppp}.

Techniques based on particle imaging are capable of capturing instantaneous snapshots of the 3D flow. In MRV, on the other hand, the measurement is the result of either ensemble or phase-locked average (for periodic flows). Allowing for long acquisition times leads to increase in *SNR* (Elkins & Alley 2007), which for a desired level of accuracy determines the spatial resolution, leading to high *DSR* on the mean flow. MRV spatial resolution typically ranges from 0.4 mm to 1 mm, over volumes often exceeding 20 cm of maximum extension (Cherry et al. 2008, Grundmann et al. 2012, Coletti et al. 2013a, Freudenhammer et al. 2014, Ryan et al. 2016).

Even optical techniques can be applied in a similar fashion, i.e. focusing only on ensemble-averaged statistics from the entire time series, with consequent improvement in resolution. In 2D imaging, this strategy has been implemented for both PIV (Westerweel et al. 2004) and PTV (Cowen and Monismith 1997, Kähler et al. 2012b), with resolutions theoretically limited by the particle image size and particle location accuracy, respectively. The latter approach has been recently extended to volumetric measurements by Agüera et al. (2016) who reached DSR = 42 using interrogation windows of (24 pixel)[3] on a dataset of 49000 snapshots. This resolution was chosen to obtain accurate Reynolds stresses; (8 pixel)[3] would be sufficient for reliable mean velocity, yielding DSR = 126.

Table 1 List of the applications included in Figure 15. CC indicates reconstruction based on cross-correlation, and LSM on least-square method. PT stands for particle tracking,

	Technique	Application	Fluid	Volume $\Delta x \times \Delta y \times \Delta z$ [mm] (full size in cm^3)
Brücker (1995)	Scanning PIV + 2D CC	Cylinder wake	Water	$66 \times 44 \times 45$ (130.7)
Hori & Sakakibara (2004)	Scanning Stereo-PIV + 2D CC	Laminar jet	Water	$100 \times 100 \times 100$ (1000.0)
David et al (2012)	Scanning Tomo-PIV + 3D CC	Flapping wing	Water	$185 \times 140 \times 83$ (2149.7)
Brücker et al (2013)	Scanning PIV + 3D LSM	Ring vortex	Water	$75 \times 75 \times 50$ (281.2)
Casey et al (2013)	Scanning Tomo-PIV + 3D CC	Turbulent jet	Water	$100 \times 100 \times 100$ (1000.0)
Lawson & Dawson (2014)	Scanning Tomo-PIV + 3D CC	Von Karman flow	Water	$125.5 \times 123.4 \times 23.5$ (363.9)
Sun & Brücker (2017)	Scanning Tomo-PIV + 3D CC	Ring vortex	Water	$70 \times 52 \times 50$ (182.0)
Elsinga et al (2006)	Tomo-PIV	Cylinder wake	Water	$40 \times 40 \times 10$ (16.0)
Hain et al (2008)	Tomo-PIV	Finite cylinder	Water	$70 \times 51.2 \times 12$ (43.0)
Atkinson et al (2011)	Tomo-PIV	Turbulent boundary layer	Air	$60 \times 60 \times 9$ (32.4)
Buchmann et al (2011)	Tomo-PIV	Carotid arthery bifurcation	Glycerin + water	$22 \times 24 \times 13$ (6.9)
Ghaemi & Scarano (2011)	Tomo-PIV	Trailing edge	Air	$47 \times 47 \times 8$ (17.7)
Kühn et al (2011)	Tomo-PIV	Convection cell	Air	$750 \times 450 \times 165$ (55687.5)
Buchner et al (2012)	Tomo-PIV	Pitching plate	Water	$85 \times 120 \times 12$ (122.4)
Violato & Scarano (2013)	Tomo-PIV	Transitional jet	Water	$33 \times 100 \times 33$ (108.9)
Ceglia et al (2014)	Tomo-PIV	Turbulent swirling jet	Water	$128 \times 128 \times 46$ (735.7)
Cafiero et al (2015)	Tomo-PIV	Jet with fractal grids	Air	$30 \times 30 \times 9$ (8.1)
Caridi et al (2016)	Tomo-PIV	Vertical axis wind turbine	Air	$400 \times 200 \times 150$ (12000.0)
Jodai & Elsinga (2016)	Tomo-PIV	Turbulent boundary layer	Water	$60 \times 55 \times 14.5$ (47.9)
Troolin & Longmire (2010)	DDPIV + PT	Vortex rings	Water	$140 \times 140 \times 120$ (2352)
Chamorro et al (2013)	DDPIV + PT	Axial-flow hydrokinetic turbine	Water	$120 \times 140 \times 60$ (1008)
Kim et al (2013)	DDPIV + PT	Clapping plates	Water	$160 \times 160 \times 160$ (4096)
Bartol et al (2016)	DDPIV + PT	Swimming squid	Water	$140 \times 140 \times 100$ (1960)
Boushaki et al (2017)	DDPIV + PT	Turbulent swirling jet	Air	$50 \times 50 \times 22$ (55)
Lüthi et al (2005)	Triangulation + LPT	Homogeneous isotropic turbulence	Water	$20 \times 15 \times 15$ (4.5)
Ouellette et al (2006)	Triangulation + LPT	Von Karman flow	Water	$50 \times 50 \times 50$ (125)
Holzner et al (2008)	Scanning triangulation + LPT	Turbulent/non-turbulent interface	Water	$20 \times 20 \times 15$ (6)
Schröder et al (2015)	Shake-the-box	Periodic hill	Water	$90 \times 94 \times 20$ (169.2)
Neeteson et al (2016)	Shake-the-box	Free-falling sphere	Water	$80 \times 68 \times 80$ (435.2)
Belden et al (2010)	Synthetic aperture PIV + 3D CC	Vortex ring	Water	$40 \times 65 \times 32$ (83.2)
Langley et al (2014)	Synthetic aperture PIV + 3D CC	Flapping wing	Water	$248 \times 48 \times 28$ (333.3)
Mendelson & Techet (2015)	Synthetic aperture PIV + 3D CC	Swimming fish	Water	$70 \times 60 \times 40$ (168)
Fahringer et al (2015)	Plenoptic PIV + 3D CC	Cylinder wake	Water	$40 \times 26.7 \times 20$ (21.4)
Meng et al (2004)	Digital Holo-PIV + PT	Cylinder wake	Water	$6.86 \times 6.86 \times 25.4$ (1.2)
Sheng et al (2008)	Digital Holo-PIV + PT	Smooth channel flow	Water	$1.5 \times 1.5 \times 2.5$ ($5.6 \cdot 10^{-3}$)
Talapatra & Katz (2012)	Digital Holo-PIV + PT	Rough channel flow	NaI + water	$3.1 \times 2.1 \times 1.8$ ($11.7 \cdot 10^{-3}$)
Toloui et al (2017)	Digital Holo-PIV + PT	Rough channel flow	NaI + water	$14.7 \times 14.4 \times 50$ (10.6)

In the above we have not explicitly addressed the Dynamic Velocity Range (DVR), i.e. the ratio of the maximum measurable velocity to the expected error. The question of the uncertainty is a subject of great scrutiny in the planar velocimetry community (Kähler et al. 2012b, Charonko & Vlachos 2013, Sciacchitano et al. 2015, Wieneke 2015). There have been studies focused on accuracy of volumetric velocimetry in specific cases, e.g. turbulent boundary layer measurements by Tomographic PIV (Atkinson et al. 2011) and Tomographic PTV (Schneiders et al. 2017), and comparisons between MRI and 2D PIV for specific configurations (Elkins et al. 2009, Coletti et al. 2013a, Töger et al. 2016). However, the systematic assessment of uncertainty of volumetric techniques is still in its infancy and will likely be a topic of high significance as the tools gain widespread use.

3.3 Evolution and technological trends

Ultimately, Eq. (6) underscores how, for a given set of experimental parameters, the resolution of particle-based volumetric velocimetry is strictly dependent on sensor size and particle image density. The available camera size has increased steadily but slowly in the last decades, although 29 Megapixel cameras are now available (a significant improvement from the 14 Megapixels mentioned by Westerweel et al. 2013). As for particle image density, the latest achievements in Tomographic PIV and LPT have shown successful reconstructions above 0.1 ppp. Since particles need be distinguishable to achieve sub-pixel location accuracy, much higher densities seem unlikely with the present sensor designs. However, such values already enable resolving fine-scale quantities such as dissipation and vorticity in laboratory flows at relatively high Reynolds numbers (Schröder et al. 2015, Schneiders et al. 2017). Assuming an appropriate uncertainty assessment establishes the validity of these new approaches in a wide variety of configurations, such a transformative capability may open previously unthinkable scenarios, and benefit the experimental and computational communities alike. In fact, as of today, the advancements in our understanding of fundamental fluid mechanics brought by volumetric velocimetry have not been proportioned to the enabled capabilities. As these become more widely available and robustly verified, much greater progresses are expected. We barely started reaping the fruits, and the present day resembles the explosion of high-speed imaging that allowed LPT to break grounds in fundamental turbulence since the early 2000s (Voth et al. 2002).

The apparent benefits of time-resolved recordings in 3D particle velocimetry brings forward a possibly more stringent constraint than the sensor size: data rate. Presently kHz acquisitions are limited to 4-Megapixel cameras, and significant technological advancements are needed to push the envelope further. Efficient data storage also becomes necessary, and compression strategies (e.g., saving only particle locations and features instead of full images, as proposed by Chan et al. 2007) are likely to become routinely adopted to increase the recording duration.

These considerations go along with the increasing capability of probing spatio-temporal fields enabled by high-speed volumetric velocimetry. Figure 16 illustrates, for a number of techniques (see applications list in Table 2), the recent trend in terms of measured velocity vectors per physical unit time (e.g.: a field of 100 vectors sampled at 1 kHz amounts to 10^5 vector/s). We assume no window overlap and do not include measurements obtained in pulse-burst mode. After a steady growth, the vector data rate of time-resolved 2D PIV has reached a plateau, surpassed by the latest implementation of Tomographic PIV, LPT, and Holographic PIV. This progress has been (and will continue to be) sustained not only by improved measurement techniques, but also by advances in data capturing, transferring, and storing.

With the increase of data sizes, efficient algorithms for reconstruction and motion analysis are increasingly important, and have long been recognized as a priority, e.g. in Tomographic PIV (Atkinson & Soria 2009, Discetti & Astarita 2012b, Lynch & Scarano 2015) and even more in MRI, where the compressed sensing paradigm is regularly used even in the acquisition step (Lustig et al. 2007, Gamper et al. 2008). Still, the number of operations required to process large data sets is unavoidably large. Therefore, GPU implementations may become the standard, and have already been adopted by several groups (Champagnat et al. 2014, Toloui et al. 2017, Bajpayee & Techet 2017). Historically, parallel computing has been minimally exploited by the experimental fluid mechanics community compared to its numerical counterpart. This might change if the recent and future advances are to be fully exploited. We remark that the increase in spatio-temporal resolution, and consequently of the amount of data, is evident both in optical and medical imaging. For example, in MRI the goal of reaching sufficient resolution to study *in vivo* hemodynamics and functional brain activity drives a continuous push for higher magnetic field strength (now exceeding 10 T in full-body scanners, Ertürk et al. 2017).
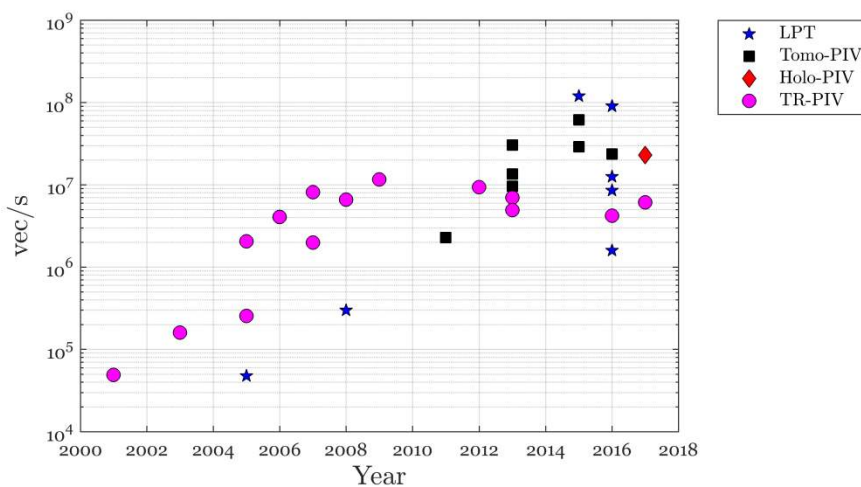

Figure 16 Historical trend of measured velocity vectors per physical unit time. Selected applications listed in Table 2.

Table 2 Panel of applications included in Figure 16. TR stands for Time-Resolved.

	Technique	Application	Fluid
Sung & Yoo (2001)	TR-PIV	Cylinder wake	Water
Van Doorne et al (2003)	TR-PIV	Pipe flow	Water
Druault et al (2005)	TR-PIV	IC engine	Air
Fore et al (2005)	TR-PIV	Wall-Mounted cube	Water
Troolin et al (2006)	TR-PIV	Gurney flap	Air
Ganapathisubramani et al (2007)	TR-PIV	Turbulent jet	Air
Wernet (2007)	TR-PIV	Jet flow	Air
Hain et al (2008)	TR-PIV	Finite cylinder	Water
Falchi & Romano (2009)	TR-PIV	Turbulent jet	Water
Scarano & Moore (2012)	TR-PIV	Trailing edge flow	Air
Oxlade et al (2012)	TR-PIV	Grid turbulence	Air
Coletti et al (2013b)	TR-PIV	Ribbed channel	Air
Immer et al (2016)	TR-PIV	Cavity flow	Air
Lian et al (2017)	TR-PIV	Homogeneous turbulence	Air
Schröder et al (2011)	TR Tomo-PIV	Turbulent boundary layer	Water
Probsting et al (2013)	TR Tomo-PIV	Turbulent boundary layer	Air
Ghaemi & Scarano (2013)	TR Tomo-PIV	Turbulent boundary layer	Air
Violato & Scarano (2013)	TR Tomo-PIV	Jet flow	Water
Probsting et al (2015)	TR Tomo-PIV	Trailing edge	Air
Zhang et al (2015)	TR Tomo-PIV	Channel flow	Water
Jodai & Elsinga (2016)	TR Tomo-PIV	Turbulent boundary layer	Water
Lüthi et al (2005)	LPT	Homogeneous turbulence	Air
Holzner et al (2008)	LPT	Turbulent/non-turbulent interface	Air
Schröder et al (2015)	Shake-the-box	Periodic hill	Water
Schanz et al (2016)	Shake-the-box	Transitional jet	Water
Schröder et al (2016)	Shake-the-box	Turbulent boundary layer	Air
Neeteson et al (2016)	Shake-the-box	Free falling sphere	Water
Schneiders et al (2016)	Tomo-PTV	Finite cylinder	Air
Toloui et al (2017)	Digital Holo-PIV + PT	Rough channel flow	NaI+Water

3.4   Combination with flow-governing equations

An inherent advantage of measuring the complete flow field (i.e. time-resolved 3D-3C velocity distributions that ideally captures all relevant scales) is the possibility of leveraging the flow-governing equations, e.g. momentum and mass conservation. In particular, in incompressible flows, continuity can be used to eliminate the spurious velocity divergence. This is often referred to as solenoidal filtering, and several strategies have recently been proposed and demonstrated in both aerodynamic and biomedical settings (de Silva et al. 2013, Busch et al. 2013, Schiavazzi et al. 2014, Azijli & Dwight 2015, Wang et al. 2017). Techniques have also been proposed to fill spatial gaps left by non-valid (or non-reliable) measurements using an incompressible finite volume Navier–Stokes solver (Sciacchitano et al. 2012). Moreover, the effective spatio-temporal resolution can be effectively enhanced by using the measurements as initial condition to the vorticity transport equation (Schneiders et al. 2014, Schneiders & Scarano 2016).

Additionally, the forces experienced by an object immersed in a fluid (such as lift and drag) can be determined from its reaction on the flow via a control volume approach. This strategy has long been applied in planar PIV, for example for the flow around 2D airfoils and cylinders (van Oudheusden et al. 2007), and the availability of volumetric data enables its application to 3D configurations (Terra et al. 2017). Recently, high-resolution LPT has enabled the measurement of the drag on a falling sphere by direct integration of the

pressure (obtained from the fluid velocity via a fully Lagrangian approach) along the body surface (Neeteson et al. 2016).

One of the most appealing possibilities offered by the measurement of the complete flow field is the evaluation of the pressure distribution itself, which in incompressible flows is the only remaining unknown of the Navier-Stokes equations. Several approaches are possible, both for the calculation of the material derivative (in a Lagrangian or Eulerian frame of reference) and for the computation of the pressure field (by spatial integration of the pressure gradient or solution of the associated Poisson equation); see the detailed review by van Oudheusden (2013). These methods can be extended to compressible flows, eliminating the density by combining the momentum and energy equations (van Oudheusden et al. 2007). The recent improvements in performance of high-speed Tomographic PIV and LPT have led to a surge in refined methodologies to obtain the unsteady pressure field, recently assessed against synthetic data by van Gent et al. (2017). One of the most attractive avenues is the evaluation of acoustic noise, which has great technological relevance in aviation. Although the determination of the full acoustic source map is challenging (also owing to the difficulty of imposing correct boundary conditions), coupling volumetric measurements with appropriate acoustic analogies appears to be a powerful strategy (Violato & Scarano 2013).

Pressure is of the uttermost relevance also in biomedical settings, especially in cardiovascular studies. Since probe measurements *in vivo* are potentially dangerous, non-invasive methods to evaluate blood pressure using velocity fields from MRI (Tyszka et al. 2000, Ebbers et al. 2002) and ultrasound imaging (Bermejo et al. 2001, Londono-Hoyos et al. 2017) are in high demand. Similar approaches as in aerodynamic applications can be used, but with important differences: the flows of interest are "internal", and therefore the solid walls (and relative boundary conditions for integration) have a prominent impact on the entire domain; the viscous term in the momentum equation can rarely be neglected, and depending on the regime it can even be the dominant one (Schiavazzi et al. 2017); and the inflow is usually oscillatory, making the relative importance of the various terms possibly time-dependent. In general, due to the multiple steps in deducing pressure from velocity, the analysis of uncertainty and its propagation is of paramount importance in both aerodynamic (Azijli et al. 2016) and biomedical (Schiavazzi et al. 2017) applications, and will likely remain a major line of research in the future.

3.5   Medical imaging

MRI is not the only imaging technique developed and/or refined by the medical physics community that is capable of measuring volumetric velocity fields. Ultrasound imaging velocimetry (or 'echo-PIV', Kim et al. 2004, Poelma 2017) was developed as a 2D-2C technique combining ultrasound echo and image cross-correlation, often using microbubbles as tracers. It was then extended to 2D-3C (Poelma et al. 2011) and recently to fully volumetric

acquisition using matrix transducers (i.e. grids of sensor elements, Falahatpisheh & Kheradvar 2014). Moreover, using Doppler methods instead of correlation-based methods, fast plane-wave imaging combined with tomographic techniques have recently allowed *in vivo* 4D measurements at sub-mm and ms resolution (Errico et al. 2015).

X-ray imaging has also been used for fluid flow velocimetry, in particular by phase-contrast imaging, i.e. cross-correlating successive images of the Fresnel diffraction patterns generated by an incident X-ray beam on tracer particles (Lee & Kim 2003, Kastengren & Powell 2014). This has been extended by Dubsky et al. (2010, 2012) to acquire full 3D velocity fields using tomographic reconstruction based on multiple projections from a relatively small number of viewing angles. Imaging of moving tracers requires a short exposure time and so high-flux synchrotron radiation is preferred, which has limited the diffusion of the method to the groups that can access such sources. Laboratory-scale X-ray sources may be used for velocimetry, but because of their lower brilliance they are rather suitable to invesigate multiphase flows where large density variations exist, such as fluidized beds and bubbly flows (Heindel 2011). Direct velocity measurements are possible with tracking techniques (XPTV, Kertzscher et al. 2004), although reaching high spatio-temporal resolution remains a challenge due to detector capabilities and size of the radiation-absorbing particles.

In general, the diffusion of medical imaging technology to fluid mechanic applications has been hindered by the need of hardware components outside the familiar palette of tools. This may lead to the misconception that non-optical imaging is more "expensive" than optical imaging. As for MRV, it is uncommon that dedicated scanners are commissioned and built for fluid mechanics applications (although examples exist, Silva et al. 2016), and what is usually needed is access to MRI facilities where phase-contrast sequences are implemented for clinical purposes. Likewise, ultrasound image velocimetry is performed with standard medical devices. The necessary access to structures and facilities can be a limit for the engineering scientist, but also an opportunity for multi-disciplinary collaborations. In general, the unique capabilities of these techniques (especially *in vivo* and in opaque fluids), indicate how optical and non-optical approaches are to be considered complementary, rather than alternative tools for 3D velocimetry.

4. Conclusions

We have surveyed several of the techniques that have imposed themselves as prime options to measure 3D-3C flow fields. To bound the focus of the review, we have limited our attention to applications at Re >> 1, therefore not including microfluidics, which require specific considerations (Cierpka & Kähler 2012, Winer et al. 2014). The emerging picture is exciting, with a wide portfolio of approaches each having distinctive strengths and significant potential for further improvement. The extremely diverse array of recent applications

indicate that volumetric velocimetry can now be applied to most flow configurations that can be characterized by single-point or planar techniques. While performance metrics can be defined and are indeed useful, the final choice of the technique to adopt shall be guided by the specific goals of the measurement. The rise of hybrid techniques has led to sizeable advances in optical methods, with a trend towards Lagrangian approaches for the motion analysis. LPT has now reached unprecedented levels of resolution and accuracy, giving access to quantities traditionally difficult to measure, such as pressure fields and turbulent dissipation. The results of the 4th International PIV Challenge (Kähler et al. 2016) indicated that LPT approaches with intense cross-talking between reconstruction and velocity evaluation seem to have the potential to supersede cross-correlation based methods in 3D. In this rapidly evolving scenario, coordinated efforts towards a standardized uncertainty quantification of volumetric velocimetry are needed. Medical imaging is gaining favour among fluid dynamicists, although mostly within collaborative frameworks with biomedicine. This should be seen as an opportunity rather than an obstacle, because the rapid progress of medical physics, steadily fostered by well-funded healthcare initiatives worldwide, is destined to continue. Finally, we anticipate that the rapid speedup in data processing, storage, and transfer associated to volumetric velocimetry will require a paradigm shift in experimental fluid mechanics; high-performance computing may play a major role in it.

Acknowledgements

Bibliography

Adelson, E. H., & Bergen, J. R. (1991). The plenoptic function and the elements of early vision," in Computational Models of Visual Processing, pp. 3-20, MIT Press.

Adelson, E. H., & Wang, J. Y. (1992). Single lens stereo with a plenoptic camera. IEEE transactions on pattern analysis and machine intelligence, 14(2), 99-106.

Adhikari, D., & Longmire, E. K. (2012a). Infrared tomographic PIV and 3D motion tracking system applied to aquatic predator–prey interaction. Measurement Science and Technology, 24(2), 024011.

Adhikari, D., & Longmire, E. K. (2012b). Visual hull method for tomographic PIV measurement of flow around moving objects. Experiments in fluids, 53(4), 943-964.

Adhikari, D., Webster, D. R., & Yen, J. (2016). Portable tomographic PIV measurements of swimming shelled Antarctic pteropods. Experiments in Fluids, 57(12), 180.

Adrian, R. J. (1997). Dynamic ranges of velocity and spatial resolution of particle image velocimetry. Measurement Science and Technology, 8(12), 1393.

Agüera, N., Cafiero, G., Astarita, T., & Discetti, S. (2016). Ensemble 3D PTV for high resolution turbulent statistics. Measurement Science and Technology, 27(12), 124011.

Angarita-Jaimes, N., McGhee, E., Chennaoui, M., Campbell, H. I., Zhang, S., Towers, C. E., ... & Towers, D. P. (2006). Wavefront sensing for single view three-component three-dimensional flow velocimetry. Experiments in fluids, 41(6), 881-891.

Amili O., Schiavazzi D., Moen S., Jagadeesan B., Van de Moortele P.F., Coletti F. "Hemodynamics in a giant intracranial aneurysm characterized by in vitro 4D flow MRI". PLOS One, under review

Atkinson, C., & Soria, J. (2009). An efficient simultaneous reconstruction technique for tomographic particle image velocimetry. Experiments in Fluids, 47(4), 553-568.

Atkinson, C., Coudert, S., Foucaut, J. M., Stanislas, M., & Soria, J. (2011). The accuracy of tomographic particle image velocimetry for measurements of a turbulent boundary layer. Experiments in fluids, 50(4), 1031-1056.

Atkinson, C., Buchmann, N. A., Amili, O., & Soria, J. (2014). On the appropriate filtering of PIV measurements of turbulent shear flows. Experiments in fluids, 55(1), 1654.

Azijli I, Dwight RP (2015) Solenoidal filtering of volumetric velocity measurements using Gaussian process regression. Exp Fluids 56(11):1–18

Azijli, I., Sciacchitano, A., Ragni, D., Palha, A., & Dwight, R. P. (2016). A posteriori uncertainty quantification of PIV-based pressure data. Experiments in Fluids, 57(5), 72.

Bajpayee, A., & Techet, A. H. (2017). Fast volume reconstruction for 3D PIV. Experiments in Fluids, 58(8), 95.

Bartol, I. K., Krueger, P. S., Jastrebsky, R. A., Williams, S., & Thompson, J. T. (2016). Volumetric flow imaging reveals the importance of vortex ring formation in squid swimming tail-first and arms-first. Journal of Experimental Biology, 219(3), 392-403.

Belden, J., Truscott, T. T., Axiak, M. C., & Techet, A. H. (2010). Three-dimensional synthetic aperture particle image velocimetry. Measurement Science and Technology, 21(12), 125403.

Belden, J., Ravela, S., Truscott, T. T., & Techet, A. H. (2012). Three-dimensional bubble field resolution using synthetic aperture imaging: application to a plunging jet. Experiments in fluids, 53(3), 839-861.

Belden, J. (2013). Calibration of multi-camera systems with refractive interfaces. Experiments in fluids, 54(2), 1463.

Benson M (2011) Measurements of 3D velocity and scalar field for a film-cooled airfoil trailing edge. PhD dissertation, Stanford University, CA.

Bermejo J, Antoranz JC, Yotti R, Moreno M, Garcia-Fernandez MA. (2001). Spatio-temporal mapping of intracardiac pressure gradients. A solution to Euler's equation from digital postprocessing of color Doppler M-mode echocardiograms. Ultrasound Med Biol, 27:621–30.

Boushaki, T., Koched, A., Mansouri, Z., & Lespinasse, F. (2017). Volumetric velocity measurements (V3V) on turbulent swirling flows. Flow Measurement and Instrumentation, 54, 46-55.

Brücker, C. (1995). Digital-particle-image-velocimetry (DPIV) in a scanning light-sheet: 3D starting flow around a short cylinder. Experiments in Fluids, 19(4), 255-263.

Brücker, C., Hess, D.-, & Kitzhofer, J. (2013). Single-view volumetric PIV via high-resolution scanning, isotropic voxel restructuring and 3D least-squares matching (3D-LSM). Measurement Science and Technology, 24(2), 024001.

Bruschewski, M., Freudenhammer, D., Buchenberg, W. B., Schiffer, H. P., & Grundmann, S. (2016). Estimation of the measurement uncertainty in magnetic resonance velocimetry based on statistical models. Experiments in Fluids, 57(5), 83.

Buchmann, N. A., Atkinson, C., Jeremy, M. C., & Soria, J. (2011). Tomographic particle image velocimetry investigation of the flow in a modeled human carotid artery bifurcation. Experiments in fluids, 50(4), 1131-1151.

Buchner, A. J., Buchmann, N., Kilany, K., Atkinson, C., & Soria, J. (2012). Stereoscopic and tomographic PIV of a pitching plate. Experiments in fluids, 52(2), 299-314.

Busch, J., Giese, D., Wissmann, L., & Kozerke, S. (2013). Reconstruction of divergence-free velocity fields from cine 3D phase-contrast flow measurements. Magnetic resonance in medicine, 69(1), 200-210.

Cafiero, G., Discetti, S., & Astarita, T. (2015). Flow field topology of submerged jets with fractal generated turbulence. Physics of Fluids, 27(11), 115103.

Caridi, G. C. A., Ragni, D., Sciacchitano, A., & Scarano, F. (2016). HFSB-seeding for large-scale tomographic PIV in wind tunnels. Experiments in Fluids, 57(12), 190.

Casey, T. A., Sakakibara, J., & Thoroddsen, S. T. (2013). Scanning tomographic particle image velocimetry applied to a turbulent jet. Physics of fluids, 25(2), 025102.

Castrillo, G., Cafiero, G., Discetti, S., & Astarita, T. (2016). Blob-enhanced reconstruction technique. Measurement Science and Technology, 27(9), 094011.

Cebral, J. R., Mut, F., Raschi, M., Scrivano, E., Ceratto, R., Lylyk, P., & Putman, C. M. (2011). Aneurysm rupture following treatment with flow-diverting stents: computational hemodynamics analysis of treatment. American journal of neuroradiology, 32(1), 27-33.

Ceglia, G., Discetti, S., Ianiro, A., Michaelis, D., Astarita, T., & Cardone, G. (2014). Three-dimensional organization of the flow structure in a non-reactive model aero engine lean burn injection system. Experimental Thermal and Fluid Science, 52, 164-173.

Chamorro, L. P., Troolin, D. R., Lee, S. J., Arndt, R. E. A., & Sotiropoulos, F. (2013). Three-dimensional flow visualization in the wake of a miniature axial-flow hydrokinetic turbine. Experiments in fluids, 54(2), 1459.

Champagnat, F., Cornic, P., Cheminet, A., Leclaire, B., Le Besnerais, G., & Plyer, A. (2014). Tomographic PIV: particles versus blobs. Measurement Science and Technology, 25(8), 084002.

Chan, K. Y., Stich, D., & Voth, G. A. (2007). Real-time image compression for high-speed particle tracking. Review of scientific instruments, 78(2), 023704.

Charonko, J. J., & Vlachos, P. P. (2013). Estimation of uncertainty bounds for individual particle image velocimetry measurements from cross-correlation peak ratio. Measurement Science and Technology, 24(6), 065301.

Chen, S., Angarita-Jaimes, N., Angarita-Jaimes, D., Pelc, B., Greenaway, A. H., Towers, C. E., ... & Towers, D. P. (2009). Wavefront sensing for three-component three-dimensional flow velocimetry in microfluidics. Experiments in Fluids, 47(4-5), 849.

Cherry, E. M., Elkins, C. J., & Eaton, J. K. (2008). Geometric sensitivity of three-dimensional separated flows. International Journal of Heat and Fluid Flow, 29(3), 803-811.

Cierpka, C., Rossi, M., Segura, R., & Kähler, C. J. (2010a). On the calibration of astigmatism particle tracking velocimetry for microflows. Measurement Science and Technology, 22(1), 015401.

Cierpka, C., Segura, R., Hain, R., & Kähler, C. J. (2010b). A simple single camera 3C3D velocity measurement technique without errors due to depth of correlation and spatial averaging for microfluidics. Measurement Science and Technology, 21(4), 045401.

Cierpka, C., Rossi, M., Segura, R., Mastrangelo, F., & Kähler, C. J. (2012). A comparative analysis of the uncertainty of astigmatism-µPTV, stereo-µPIV, and µPIV. Experiments in fluids, 52(3), 605-615.

Cierpka, C., & Kähler, C. J. (2012). Particle imaging techniques for volumetric three-component (3D3C) velocity measurements in microfluidics. Journal of visualization, 15(1), 1-31.

Coletti, F., Elkins, C. J., & Eaton, J. K. (2013a). An inclined jet in crossflow under the effect of streamwise pressure gradients. Experiments in fluids, 54(9), 1589.

Coletti, F., Cresci, I., & Arts, T. (2013b). Spatio-temporal analysis of the turbulent flow in a ribbed channel. International Journal of Heat and Fluid Flow, 44, 181-196.

Coletti, F., Muramatsu, K., Schiavazzi, D., Elkins, C. J., & Eaton, J. K. (2014). Fluid flow and scalar transport through porous fins. Physics of Fluids, 26(5), 055104.

Cowen, E. A., & Monismith, S. G. (1997). A hybrid digital particle tracking velocimetry technique. Experiments in fluids, 22(3), 199-211.

David, L., Jardin, T., Braud, P., & Farcy, A. (2012). Time-resolved scanning tomography PIV measurements around a flapping wing. Experiments in fluids, 52(4), 857-864.

de Silva, C. M., Philip, J., & Marusic, I. (2013). Minimization of divergence error in volumetric velocity measurements and implications for turbulence statistics. Experiments in fluids, 54(7), 1557.

Diez, F. J., Cheng, Y., & Villegas, A. (2011). Time resolved visualization of structures of velocity gradients measured with near Kolmogorov-scale resolution in turbulent free-shear flows. Experimental Thermal and Fluid Science, 35(6), 1223-1229.

Discetti, S., & Astarita, T. (2012a). A fast multi-resolution approach to tomographic PIV. Experiments in fluids, 52(3), 765-777.

Discetti, S., & Astarita, T. (2012b). Fast 3D PIV with direct sparse cross-correlations. Experiments in fluids, 53(5), 1437-1451.

Discetti, S., Natale, A., & Astarita, T. (2013). Spatial filtering improved tomographic PIV. Experiments in fluids, 4(54), 1-13.

Discetti, S., & Astarita, T. (2014). The detrimental effect of increasing the number of cameras on self-calibration for tomographic PIV. Measurement Science and Technology, 25(8), 084001.

Druault, P., Guibert, P., & Alizon, F. (2005). Use of proper orthogonal decomposition for time interpolation from PIV data. Experiments in Fluids, 39(6), 1009-1023

Dubsky, S., Jamison, R. A., Irvine, S. C., Siu, K. K. W., Hourigan, K., & Fouras, A. (2010). Computed tomographic x-ray velocimetry. Applied Physics Letters, 96(2), 023702.

Dubsky, S., Jamison, R. A., Higgins, S. P. A., Siu, K. K. W., Hourigan, K., & Fouras, A. (2012). Computed tomographic X-ray velocimetry for simultaneous 3D measurement of velocity and geometry in opaque vessels. Experiments in fluids, 52(3), 543-554.

Ebbers, T., Wigstrom, L., Bolger, A. F., Wranne, B., & Karlsson, M. (2002). Noninvasive measurement of time-varying three-dimensional relative pressure fields within the human heart. Journal of biomechanical engineering, 124(3), 288-293.

Elkins, C. J., & Alley, M. T. (2007). Magnetic resonance velocimetry: applications of magnetic resonance imaging in the measurement of fluid motion. Experiments in Fluids, 43(6), 823-858.

Elkins, C. J., Alley, M. T., Saetran, L., & Eaton, J. K. (2009). Three-dimensional magnetic resonance velocimetry measurements of turbulence quantities in complex flow. Experiments in Fluids, 46(2), 285-296.

Elsinga, G. E., Scarano, F., Wieneke, B., & van Oudheusden, B. W. (2006). Tomographic particle image velocimetry. Experiments in fluids, 41(6), 933-947.

Elsinga, G. E., Westerweel, J., Scarano, F., & Novara, M. (2011). On the velocity of ghost particles and the bias errors in Tomographic-PIV. Experiments in fluids, 50(4), 825-838.

Errico, C., Pierre, J., Pezet, S., Desailly, Y., Lenkei, Z., Couture, O., & Tanter, M. (2015). Ultrafast ultrasound localization microscopy for deep super-resolution vascular imaging. Nature, 527(7579), 499.

Ertürk, M. A., Wu, X., Eryaman, Y., Moortele, P. F., Auerbach, E. J., Lagore, R. L., ... & Metzger, G. J. (2017). Toward imaging the body at 10.5 tesla. Magnetic resonance in medicine, 77(1), 434-443.

Fahringer, T. W., Lynch, K. P., & Thurow, B. S. (2015). Volumetric particle image velocimetry with a single plenoptic camera. Measurement Science and Technology, 26(11), 115201.

Falahatpisheh A, Kheradvar A (2014) Volumetric echocardiographic particle image velocimetry (V-Echo-PIV). Circulation 130(Suppl 2):A14952–A14952.

Falchi, M., & Romano, G. P. (2009). Evaluation of the performance of high-speed PIV compared to standard PIV in a turbulent jet. Experiments in fluids, 47(3), 509-526.

Fore, L. B., Tung, A. T., Buchanan, J. R., & Welch, J. W. (2005). Nonlinear temporal filtering of time-resolved digital particle image velocimetry data. Experiments in fluids, 39(1), 22-31.

Foucaut, J. M., Carlier, J., & Stanislas, M. (2004). PIV optimization for the study of turbulent flow using spectral analysis. Measurement Science and Technology, 15(6), 1046.

Freudenhammer, D., Baum, E., Peterson, B., Böhm, B., Jung, B., & Grundmann, S. (2014). Volumetric intake flow measurements of an IC engine using magnetic resonance velocimetry. Experiments in Fluids, 55(5), 1724.

Fukushima, E. (1999). Nuclear magnetic resonance as a tool to study flow. Annual review of fluid mechanics, 31(1), 95-123.

Gabor, D. (1948). A new microscopic principle. Nature, 161(4098), 777-778.

Ganapathisubramani, B., Lakshminarasimhan, K., & Clemens, N. T. (2007). Determination of complete velocity gradient tensor by using cinematographic stereoscopic PIV in a turbulent jet. Experiments in fluids, 42(6), 923-939.

Gamper, U., Boesiger, P., & Kozerke, S. (2008). Compressed sensing in dynamic MRI. Magnetic resonance in medicine, 59(2), 365-373.

Gesemann, S. (2015). From particle tracks to velocity and acceleration fields using B-splines and penalties. arXiv preprint arXiv:1510.09034.

Ghaemi, S., & Scarano, F. (2010). Multi-pass light amplification for tomographic particle image velocimetry applications. Measurement Science and Technology, 21(12), 127002.

Ghaemi, S., & Scarano, F. (2011). Counter-hairpin vortices in the turbulent wake of a sharp trailing edge. Journal of Fluid Mechanics, 689, 317-356.

Ghaemi, S., & Scarano, F. (2013). Turbulent structure of high-amplitude pressure peaks within the turbulent boundary layer. Journal of Fluid Mechanics, 735, 381-426.

Gopalan, B., Malkiel, E., & Katz, J. (2008). Experimental investigation of turbulent diffusion of slightly buoyant droplets in locally isotropic turbulence. Physics of Fluids, 20(9), 095102.

Griswold, M. A., Jakob, P. M., Heidemann, R. M., Nittka, M., Jellus, V., Wang, J., ... & Haase, A. (2002). Generalized autocalibrating partially parallel acquisitions (GRAPPA). Magnetic resonance in medicine, 47(6), 1202-1210.

Grothe, R. L., & Dabiri, D. (2008). An improved three-dimensional characterization of defocusing digital particle image velocimetry (DDPIV) based on a new imaging volume definition. Measurement Science and Technology, 19(6), 065402.

Grundmann, S., Wassermann, F., Lorenz, R., Jung, B., & Tropea, C. (2012). Experimental investigation of helical structures in swirling flows. International Journal of Heat and Fluid Flow, 37, 51-63.

Haacke, E. M., Smith, A. S., Lin, W., Lewin, J. S., Finelli, D. A., & Duerk, J. L. (1991). Velocity quantification in magnetic resonance imaging. Topics in Magnetic Resonance Imaging, 3(3), 34-49.

Hain, R., Kähler, C. J., & Michaelis, D. (2008). Tomographic and time resolved PIV measurements on a finite cylinder mounted on a flat plate. Experiments in fluids, 45(4), 715-724.

Heindel, T. J. (2011). A review of X-ray flow visualization with applications to multiphase flows. Journal of Fluids Engineering, 133(7), 074001.

Herman, G. T., & Lent, A. (1976). Iterative reconstruction algorithms. Computers in biology and medicine, 6(4), 273-294.

Hinsch, K. D. (2002). Holographic particle image velocimetry. Measurement Science and Technology, 13(7), R61.

Hori, T., & Sakakibara, J. (2004). High-speed scanning stereoscopic PIV for 3D vorticity measurement in liquids. Measurement Science and Technology, 15(6), 1067.

Holzner, M., Liberzon, A., Nikitin, N., Lüthi, B., Kinzelbach, W., & Tsinober, A. (2008). A Lagrangian investigation of the small-scale features of turbulent entrainment through particle tracking and direct numerical simulation. Journal of Fluid Mechanics, 598, 465-475.

Hunt, J. C., Wray, A. A., & Moin, P. (1988). Eddies, streams, and convergence zones in turbulent flows.

Immer, M., Allegrini, J., & Carmeliet, J. (2016). Time-resolved and time-averaged stereo-PIV measurements of a unit-ratio cavity. Experiments in Fluids, 57(6), 101.

Jalal, S., Nemes, A., Van de Moortele, T., Schmitter, S., & Coletti, F. (2016). Three-dimensional inspiratory flow in a double bifurcation airway model. Experiments in Fluids, 57(9), 148.

Jodai, Y., & Elsinga, G. E. (2016). Experimental observation of hairpin auto-generation events in a turbulent boundary layer. Journal of Fluid Mechanics, 795, 611-633.

Kähler, C. J., Scharnowski, S., & Cierpka, C. (2012a). On the resolution limit of digital particle image velocimetry. Experiments in fluids, 52(6), 1629-1639.

Kähler, C. J., Scharnowski, S., & Cierpka, C. (2012b). On the uncertainty of digital PIV and PTV near walls. Experiments in fluids, 52(6), 1641-1656.

Kähler, C. J., Astarita, T., Vlachos, P. P., Sakakibara, J., Hain, R., Discetti, S., ... & Cierpka, C. (2016). Main results of the 4th International PIV Challenge. Experiments in Fluids, 57(6), 97.

Kajitani, L., & Dabiri, D. (2005). A full three-dimensional characterization of defocusing digital particle image velocimetry. Measurement Science and Technology, 16(3), 790.

Kao, H. P., & Verkman, A. S. (1994). Tracking of single fluorescent particles in three dimensions: use of cylindrical optics to encode particle position. Biophysical journal, 67(3), 1291-1300.

Kastengren, A., & Powell, C. F. (2014). Synchrotron X-ray techniques for fluid dynamics. Experiments in fluids, 55(3), 1686.

Katz, J., & Sheng, J. (2010). Applications of holography in fluid mechanics and particle dynamics. Annual Review of Fluid Mechanics, 42, 531-555.

Kertzscher, U., Seeger, A., Affeld, K., Goubergrits, L., & Wellnhofer, E. (2004). X-ray based particle tracking velocimetry–a measurement technique for multi-phase flows and flows without optical access. Flow Measurement and Instrumentation, 15(4), 199-206.

Kim, H., J. Hertzberg, and R. Shandas. (2004) Development and validation of echo PIV. Experiments in Fluids 36:455–462.

Kim, D., Hussain, F., & Gharib, M. (2013). Vortex dynamics of clapping plates. Journal of Fluid Mechanics, 714, 5-23.

Kühn, M., Ehrenfried, K., Bosbach, J., & Wagner, C. (2011). Large-scale tomographic particle image velocimetry using helium-filled soap bubbles. Experiments in fluids, 50(4), 929-948.

Langley, K. R., Hardester, E., Thomson, S. L., & Truscott, T. T. (2014). Three-dimensional flow measurements on flapping wings using synthetic aperture PIV. Experiments in fluids, 55(10), 1831.

Latychevskaia, T., Gehri, F., & Fink, H. W. (2010). Depth-resolved holographic reconstructions by three-dimensional deconvolution. Optics express, 18(21), 22527-22544.

Lawson, J. M., & Dawson, J. R. (2014). A scanning PIV method for fine-scale turbulence measurements. Experiments in fluids, 55(12), 1857.

Lee, S. J., & Kim, G. B. (2003). X-ray particle image velocimetry for measuring quantitative flow information inside opaque objects. Journal of Applied Physics, 94(5), 3620-3623.

Levoy, M. (2006). Light fields and computational imaging. Computer, 39(8), 46-55.

Lian, H., Soulopoulos, N., & Hardalupas, Y. (2017). Evaluation of the topological characteristics of the turbulent flow in a 'box of turbulence' through 2D time-resolved particle image velocimetry. Experiments in Fluids, 58(9), 118.

Lin, D., Angarita-Jaimes, N. C., Chen, S., Greenaway, A. H., Towers, C. E., & Towers, D. P. (2008). Three-dimensional particle imaging by defocusing method with an annular aperture. Optics letters, 33(9), 905-907.

Londono-Hoyos, F. J., Swillens, A., Van Cauwenberge, J., Meyers, B., Koppula, M. R., Vlachos, P., ... & Segers, P. (2017). Assessment of methodologies to calculate intraventricular pressure differences in computational models and patients. Medical & Biological Engineering & Computing, 1-13.

Lu, J., Fugal, J. P., Nordsiek, H., Saw, E. W., Shaw, R. A., & Yang, W. (2008). Lagrangian particle tracking in three dimensions via single-camera in-line digital holography. New Journal of Physics, 10(12), 125013.

Lustig, M., Donoho, D., & Pauly, J. M. (2007). Sparse MRI: The application of compressed sensing for rapid MR imaging. Magnetic resonance in medicine, 58(6), 1182-1195.

Lynch, K. P., & Scarano, F. (2015). An efficient and accurate approach to MTE-MART for time-resolved tomographic PIV. Experiments in Fluids, 3(56), 1-16.

Lüthi, B., Tsinober, A., & Kinzelbach, W. (2005). Lagrangian measurement of vorticity dynamics in turbulent flow. Journal of Fluid mechanics, 528, 87-118.

Maas, H. G., Gruen, A., & Papantoniou, D. (1993). Particle tracking velocimetry in three-dimensional flows. Experiments in Fluids, 15(2), 133-146.

Maas, H. G., Westfeld, P., Putze, T., Bøtkjær, N., Kitzhofer, J., & Brücker, C. (2009). Photogrammetric techniques in multi-camera tomographic PIV. In Proceedings of the 8th International Symposium on Particle Image Velocimetry (pp. 25-28).

Markl, M., Chan, F. P., Alley, M. T., Wedding, K. L., Draney, M. T., Elkins, C. J., ... & Pelc, N. J. (2003). Time-resolved three-dimensional phase-contrast MRI. Journal of Magnetic Resonance Imaging, 17(4), 499-506.

Markl, M., Frydrychowicz, A., Kozerke, S., Hope, M., & Wieben, O. (2012). 4D flow MRI. Journal of Magnetic Resonance Imaging, 36(5), 1015-1036.

Mendelson, L., & Techet, A. H. (2015). Quantitative wake analysis of a freely swimming fish using 3D synthetic aperture PIV. Experiments in Fluids, 56(7), 135.

Meng, H., Pan, G., Pu, Y., & Woodward, S. H. (2004). Holographic particle image velocimetry: from film to digital recording. Measurement Science and Technology, 15(4), 673.

Mendez, M. A., Raiola, M., Masullo, A., Discetti, S., Ianiro, A., Theunissen, R., & Buchlin, J. M. (2017). POD-based background removal for particle image velocimetry. Experimental Thermal and Fluid Science, 80, 181-192.

Mishra, D., Muralidhar, K., & Munshi, P. (1999). A robust MART algorithm for tomographic applications. Numerical Heat Transfer: Part B: Fundamentals, 35(4), 485-506.

Mordant, N., Crawford, A. M., & Bodenschatz, E. (2004). Experimental Lagrangian acceleration probability density function measurement. Physica D: Nonlinear Phenomena, 193(1), 245-251.

Murphy, D. W., Webster, D. R., & Yen, J. (2013). The hydrodynamics of hovering in Antarctic krill. Limnology and Oceanography: Fluids and Environments, 3(1), 240-255.

Neeteson, N. J., Bhattacharya, S., Rival, D. E., Michaelis, D., Schanz, D., & Schröder, A. (2016). Pressure-field extraction from Lagrangian flow measurements: first experiences with 4D-PTV data. Experiments in Fluids, 57(6), 102.

Nishino, K., Kasagi, N., Hirata, M. (1989) Three-dimensional particle tracking velocimetry based on automated digital image processing. Trans ASME J Fluid Eng 111:384–390.

Novara, M., Batenburg, K. J., & Scarano, F. (2010). Motion tracking-enhanced MART for tomographic PIV. Measurement science and technology, 21(3), 035401.

Novara, M., & Scarano, F. (2012). Performances of motion tracking enhanced Tomographic PIV on turbulent shear flows. Experiments in fluids, 52(4), 1027-1041.

Novara, M., & Scarano, F. (2013). A particle-tracking approach for accurate material derivative measurements with tomographic PIV. Experiments in fluids, 54(8), 1584.

Novara, M., Schanz, D., Reuther, N., Kähler, C. J., & Schröder, A. (2016). Lagrangian 3D particle tracking in high-speed flows: Shake-The-Box for multi-pulse systems. Experiments in Fluids, 57(8), 128.

Ouellette, N. T., Xu, H., & Bodenschatz, E. (2006). A quantitative study of three-dimensional Lagrangian particle tracking algorithms. Experiments in Fluids, 40(2), 301-313.

Oxlade, A. R., Valente, P. C., Ganapathisubramani, B., & Morrison, J. F. (2012). Denoising of time-resolved PIV for accurate measurement of turbulence spectra and reduced error in derivatives. Experiments in fluids, 53(5), 1561-1575.

Pelc, N. J., Sommer, F. G., Li, K. C., Brosnan, T. J., Herfkens, R. J., & Enzmann, D. R. (1994). Quantitative magnetic resonance flow imaging. Magnetic resonance quarterly, 10(3), 125-147.

Pereira, F., Gharib, M., Dabiri, D., & Modarress, D. (2000). Defocusing digital particle image velocimetry: a 3-component 3-dimensional DPIV measurement technique. Application to bubbly flows. Experiments in Fluids, 29, S078-S084.

Pereira, F., & Gharib, M. (2002). Defocusing digital particle image velocimetry and the three-dimensional characterization of two-phase flows. Measurement Science and Technology, 13(5), 683.

Pereira, F., Stüer, H., Graff, E. C., & Gharib, M. (2006). Two-frame 3D particle tracking. Measurement science and technology, 17(7), 1680.

Poelma, C., Mari, J. M., Foin, N., Tang, M. X., Krams, R., Caro, C. G., ... & Westerweel, J. (2011). 3D Flow reconstruction using ultrasound PIV. Experiments in fluids, 50(4), 777-785.

Poelma, C. (2017). Ultrasound imaging velocimetry: a review. Experiments in Fluids, 58(1), 3.

Ponitz, B., Sastuba, M., Brücker, C., & Kitzhofer, J. (2012). Volumetric velocimetry via scanning back-projection and least-squares-matching algorithms of a vortex ring. In 16th International symposium on applications of laser techniques to fluid mechanics. ISBN (pp. 978-989).

Ponitz, B., Sastuba, M., & Brücker, C. (2016). 4D visualization study of a vortex ring life cycle using modal analyses. Journal of Visualization, 19(2), 237-259.

Pröbsting, S., Scarano, F., Bernardini, M., & Pirozzoli, S. (2013). On the estimation of wall pressure coherence using time-resolved tomographic PIV. Experiments in fluids, 54(7), 1567.

Pröbsting, S., Tuinstra, M., & Scarano, F. (2015). Trailing edge noise estimation by tomographic particle image velocimetry. Journal of Sound and Vibration, 346, 117-138.

Raffel, M., Willert, C. E., & Kompenhans, J. (2007). Particle image velocimetry: a practical guide. Springer Science & Business Media.

Ryan, K. J., Coletti, F., Elkins, C. J., Dabiri, J. O., & Eaton, J. K. (2016). Three-dimensional flow field around and downstream of a subscale model rotating vertical axis wind turbine. Experiments in Fluids, 57(3), 38.

Scarano, F. (2001). Iterative image deformation methods in PIV. Measurement science and technology, 13(1), R1.

Scarano, F., & Moore, P. (2012). An advection-based model to increase the temporal resolution of PIV time series. Experiments in fluids, 52(4), 919-933. Sung, J., & Yoo, J. Y. (2001). Three-dimensional phase averaging of time-resolved PIV measurement data. Measurement Science and Technology, 12(6), 655.

Scarano, F. (2013). Tomographic PIV: principles and practice. Measurement Science and Technology, 24(1), 012001.

Schanz, D., Gesemann, S., Schröder, A., Wieneke, B., & Novara, M. (2012). Non-uniform optical transfer functions in particle imaging: calibration and application to tomographic reconstruction. Measurement Science and Technology, 24(2), 024009.

Schanz, D., Gesemann, S., & Schröder, A. (2016). Shake-The-Box: Lagrangian particle tracking at high particle image densities. Experiments in fluids, 57(5), 70.

Schiavazzi, D., Coletti, F., Iaccarino, G., & Eaton, J. K. (2014). A matching pursuit approach to solenoidal filtering of three-dimensional velocity measurements. Journal of Computational Physics, 263, 206-221.

Schiavazzi, D. E., Nemes, A., Schmitter, S., & Coletti, F. (2017). The effect of velocity filtering in pressure estimation. Experiments in Fluids, 58(5), 50.

Schneiders, J. F., Dwight, R. P., & Scarano, F. (2014). Time-supersampling of 3D-PIV measurements with vortex-in-cell simulation. Experiments in Fluids, 55(3), 1692.

Schneiders, J. F., & Scarano, F. (2016). Dense velocity reconstruction from tomographic PTV with material derivatives. Experiments in Fluids, 57(9), 139.

Schneiders, J. F., Scarano, F., & Elsinga, G. E. (2017). Resolving vorticity and dissipation in a turbulent boundary layer by tomographic PTV and VIC+. Experiments in Fluids, 58(4), 27.

Sciacchitano, A., Dwight, R. P., & Scarano, F. (2012). Navier–Stokes simulations in gappy PIV data. Experiments in fluids, 53(5), 1421-1435.

Sciacchitano, A., Neal, D. R., Smith, B. L., Warner, S. O., Vlachos, P. P., Wieneke, B., & Scarano, F. (2015). Collaborative framework for PIV uncertainty quantification: comparative assessment of methods. Measurement Science and Technology, 26(7), 074004.

Schröder, A., Geisler, R., Staack, K., Elsinga, G. E., Scarano, F., Wieneke, B., ... & Westerweel, J. (2011). Eulerian and Lagrangian views of a turbulent boundary layer flow using time-resolved tomographic PIV. Experiments in fluids, 50(4), 1071-1091.

Schröder, A., Schanz, D., Michaelis, D., Cierpka, C., Scharnowski, S., & Kähler, C. J. (2015). Advances of PIV and 4D-PTV" Shake-The-Box" for Turbulent Flow Analysis–the Flow over Periodic Hills. Flow, Turbulence and Combustion, 95(2-3), 193-209.

Schröder, A., Schanz, D., Geisler, R., & Gesemann, S. (2016). Investigations of coherent structures in near-wall turbulence and large wall-shear stress events using Shake-The-Box.

Sheng, J., Malkiel, E., & Katz, J. (2008). Using digital holographic microscopy for simultaneous measurements of 3D near wall velocity and wall shear stress in a turbulent boundary layer. Experiments in fluids, 45(6), 1023-1035.

Shi, S., Ding, J., New, T. H., & Soria, J. (2017). Light-field camera-based 3D volumetric particle image velocimetry with dense ray tracing reconstruction technique. Experiments in Fluids, 58(7), 78.

Silva, R., Garcia, F. A. P., Faia, P. M., Krochak, P., Söderberg, D., Lundell, F., & Rasteiro, M. G. (2016). Validating dilute settling suspensions numerical data through MRI, UVP and EIT measurements. Flow Measurement and Instrumentation, 50, 35-48.

Soria, J., & Atkinson, C. (2008). Towards 3C-3D digital holographic fluid velocity vector field measurement—tomographic digital holographic PIV (Tomo-HPIV). Measurement science and technology, 19(7), 074002.

Steinman, D. A., Hoi, Y., Fahy, P., Morris, L., Walsh, M. T., Aristokleous, N., ... & Berg, P. (2013). Variability of computational fluid dynamics solutions for pressure and flow in a giant aneurysm: the ASME 2012 Summer Bioengineering Conference CFD Challenge. Journal of biomechanical engineering, 135(2), 021016.

Sun, Z., & Brücker, C. (2017). Investigation of the vortex ring transition using scanning Tomographic PIV. Experiments in Fluids, 58(4), 36.

Sung, J., & Yoo, J. Y. (2001). Three-dimensional phase averaging of time-resolved PIV measurement data. Measurement Science and Technology, 12(6), 655.

Talapatra, S., & Katz, J. (2012). Coherent structures in the inner part of a rough-wall channel flow resolved using holographic PIV. Journal of Fluid Mechanics, 711, 161-170.

Terra, W., Sciacchitano, A., & Scarano, F. (2017). Aerodynamic drag of a transiting sphere by large-scale tomographic-PIV. Experiments in Fluids, 58(7), 83.

Töger, J., Bidhult, S., Revstedt, J., Carlsson, M., Arheden, H., & Heiberg, E. (2016). Independent validation of four-dimensional flow MR velocities and vortex ring volume using particle imaging velocimetry and planar laser-Induced fluorescence. Magnetic resonance in medicine, 75(3), 1064-1075.

Toloui, M., & Hong, J. (2015). High fidelity digital inline holographic method for 3D flow measurements. Optics express, 23(21), 27159-27173.

Toloui, M., Mallery, K., & Hong, J. (2017). Improvements on digital inline holographic PTV for 3D wall-bounded turbulent flow measurements. Measurement Science and Technology, 28(4), 044009.

Troolin, D. R., Longmire, E. K., & Lai, W. T. (2006). Time resolved PIV analysis of flow over a NACA 0015 airfoil with Gurney flap. Experiments in Fluids, 41(2), 241-254.

Troolin, D. R., & Longmire, E. K. (2010). Volumetric velocity measurements of vortex rings from inclined exits. Experiments in fluids, 48(3), 409-420.

Tsien, W. H., Kartes, P., Yamasaki, T., & Dabiri, D. (2008). A color-coded backlighted defocusing digital particle image velocimetry system. Experiments in Fluids, 44(6), 1015-1026.

Tyszka, J. M., Laidlaw, D. H., Asa, J. W., & Silverman, J. M. (2000). Three-dimensional, time-resolved (4D) relative pressure mapping using magnetic resonance imaging. Journal of Magnetic Resonance Imaging, 12(2), 321-329.

Vaish, V., Garg, G., Talvala, E. V., Antunez, E., Wilburn, B., Horowitz, M., & Levoy, M. (2005). Synthetic aperture focusing using a shear-warp factorization of the viewing transform. In Computer Vision and Pattern Recognition-Workshops, 2005. CVPR Workshops. IEEE Computer Society Conference on (pp. 129-129). IEEE.

Van Doorne, C. W. H., Hof, B., Lindken, R. H., Westerweel, J., & Dierksheide, U. (2003). Time resolved stereoscopic PIV in pipe flow. Visualizing 3D flow structures. In Proceedings of fifth international symposium on particle image velocimetry. Busan, South-Korea, September (pp. 22-24).

van Gent, P. L., Michaelis, D., Van Oudheusden, B. W., Weiss, P. É., De Kat, R., Laskari, A., ... & Gesemann, S. (2017). Comparative assessment of pressure field reconstructions from particle image velocimetry measurements and Lagrangian particle tracking. Experiments in Fluids, 58(4), 33.

van Oudheusden, B. W. (2013). PIV-based pressure measurement. Measurement Science and Technology, 24(3), 032001.

van Oudheusden, B. W., Scarano, F., Roosenboom, E. W., Casimiri, E. W., & Souverein, L. J. (2007). Evaluation of integral forces and pressure fields from planar velocimetry data for incompressible and compressible flows. Experiments in Fluids, 43(2-3), 153-162.

Violato, D., & Scarano, F. (2013). Three-dimensional vortex analysis and aeroacoustic source characterization of jet core breakdown. Physics of fluids, 25(1), 015112.

Voth, G. A., la Porta, A., Crawford, A. M., Alexander, J., & Bodenschatz, E. (2002). Measurement of particle accelerations in fully developed turbulence. Journal of Fluid Mechanics, 469, 121-160.

Wang, C., Gao, Q., Wei, R., Li, T., & Wang, J. (2017). Weighted divergence correction scheme and its fast implementation. Experiments in Fluids, 58(5), 44.

Wassermann, F., Hecker, D., Jung, B., Markl, M., Seifert, A., & Grundmann, S. (2013). Phase-locked 3D3C-MRV measurements in a bi-stable fluidic oscillator. Experiments in fluids, 54(3), 1487.

Watanabe, R., Gono, T., Yamagata, T., & Fujisawa, N. (2015). Three-dimensional flow structure in highly buoyant jet by scanning stereo PIV combined with POD analysis. International Journal of Heat and Fluid Flow, 52, 98-110.

Wernet, M. P. (2007). Temporally resolved PIV for space–time correlations in both cold and hot jet flows. Measurement Science and Technology, 18(5), 1387.

Westerhof, N., Lankhaar, J.W., Westerhof, B., 2009. The arterial windkessel. Medical and Biological Engineering and Computing 47, 131–141.

Westerweel, J., Geelhoed, P. F., & Lindken, R. (2004). Single-pixel resolution ensemble correlation for micro-PIV applications. Experiments in Fluids, 37(3), 375-384.

Westerweel, J., & Scarano, F. (2005). Universal outlier detection for PIV data. Experiments in fluids, 39(6), 1096-1100.

Westerweel, J., Elsinga, G. E., & Adrian, R. J. (2013). Particle image velocimetry for complex and turbulent flows. Annual Review of Fluid Mechanics, 45, 409-436.

Wieneke, B. (2008). Volume self-calibration for 3D particle image velocimetry. Experiments in fluids, 45(4), 549-556.

Wieneke, B. (2013). Iterative reconstruction of volumetric particle distribution. Measurement Science and Technology, 24(2), 024008.

Wieneke, B. (2015). PIV uncertainty quantification from correlation statistics. Measurement Science and Technology, 26(7), 074002.

Willert, C. E., & Gharib, M. (1992). Three-dimensional particle imaging with a single camera. Experiments in Fluids, 12(6), 353-358.

Winer, M. H., Ahmadi, A., & Cheung, K. C. (2014). Application of a three-dimensional (3D) particle tracking method to microfluidic particle focusing. Lab on a Chip, 14(8), 1443-1451.

Xu, H., Pumir, A., Falkovich, G., Bodenschatz, E., Shats, M., Xia, H., ... & Boffetta, G. (2014). Flight–crash events in turbulence. Proceedings of the National Academy of Sciences, 111(21), 7558-7563.

Zhang, C., Miorini, R., & Katz, J. (2015). Integrating Mach–Zehnder interferometry with TPIV to measure the time-resolved deformation of a compliant wall along with the 3D velocity field in a turbulent channel flow. Experiments in Fluids, 56(11), 203.

Zhou, J., Adrian, R. J., Balachandar, S., & Kendall, T. M. (1999). Mechanisms for generating coherent packets of hairpin vortices in channel flow. Journal of fluid mechanics, 387, 353-396.